Effect of Mn Content on the Passivation and Corrosion of Al0.3Cr0.5Fe2MnxMo0.15Ni1.5Ti0.3 Compositionally Complex Face-Centered Cubic Alloys

S.B. Inman, Junsoo Han, A.Y. Gerard, J. Qi, M.A. Wischhusen, S.R. Agnew, S.J. Poon, K. Ogle, J.R. Scully

Effect of Mn Content on the Passivation and Corrosion of $Al_{0.3}Cr_{0.5}Fe_2Mn_xMo_{0.15}Ni_{1.5}Ti_{0.3}$ Compositionally Complex Face-Centered Cubic Alloys

*S.B. Inman,[‡,***] J. Han,[*********] A.Y. Gerard,[***] J. Qi,[*****] M.A. Wischhusen,[*] S.R. Agnew,[*] S.J. Poon,[*****] K. Ogle,[***] and J.R. Scully[***]*

$Al_{0.3}Cr_{0.5}Fe_2Mn_xMo_{0.15}Ni_{1.5}Ti_{0.3}$ (x = 0, 0.25, 0.5, 1) compositionally complex alloys are synthesized and annealed at 1,070°C to form two-phase alloys with a face-centered cubic (fcc) matrix and a second phases enriched in Al, Ti, and Ni with slightly reduced density, raw element costs, and passivating elements distributed across both phases. The global corrosion resistance is evaluated in 0.01 M and 0.1 M NaCl at both natural pH and pH 4. Overall corrosion resistance is suggested to be optimized at Mn concentrations of 5.0 at%, indicated by pitting potentials comparable to or exceeding those of 316L stainless steel. Improvements in corrosion resistance and optimization of Mn concentration are further assessed by polarization, impedance, and gravimetric analysis after extended aqueous exposure. The fate of individual elements during the dissolution and passivation processes is evaluated with in situ atomic emission spectroelectrochemistry and ex situ x-ray photoelectron spectroscopy. Passivity was derived from combinations of Ti^{4+}, Cr^{3+}, and Al^{3+} oxides in an undetermined solid solution or complex oxide. Enhanced corrosion resistance is attributed to the improved chemical homogeneity of passivating elements within the two-phase microstructure, while the decreased corrosion resistance of alloys with higher Mn concentrations is attributed to high Mn dissolution rates and/or destabilization of the passive films. The underlying determinants of the role of Mn in the design of corrosion-resistant lightweight compositionally complex alloys are discussed.

KEY WORDS: atomic emission spectroelectrochemistry, compositionally complex alloy, corrosion, high entropy alloy, microstructure, multi-principal element alloy, passivation, x-ray photoelectron spectroscopy

INTRODUCTION

Compositionally complex alloys (CCAs), a broad alloy class which includes high entropy alloys (HEAs) and multi-principal element alloys (MPEAs), involve combinations of four or more elements with compositions above 5 at%. Compositions may deviate from the equimolar constraints that typically define HEAs, greatly increasing the alloy compositional space.[1-2] These alloys show promise in producing superior corrosion resistance as well as other desirable properties but the ideal selection of alloying elements for a specific property has not been mastered. Moreover, low cost materials with reduced density are possible in light weight HEAs particularly with less expensive alloying elements such as Al and Fe. The high configurational entropy from multiple elements at significant concentrations increases the likelihood of overcoming enthalpy driven segregation and preserving single-phase stability.[1,3] Composition based thermodynamic parameters indicated below may be used to predict phase stability. Single-phase stability is increasingly likely with a configurational entropy (ΔS_{mix}) above 1.5R (where R is the ideal gas constant and c_i corresponds to the concentration of element i), an enthalpy of mixing (ΔH_{mix}) calculated by the Miedema model[4-5] less negative than −16.25 kJ/mol (where ΔH_{ij} corresponds to the enthalpy of mixing of elements i and j), and/or an atomic radius (r) mean squared deviation (δ) of less than 4.7%.[1]

$$\Delta S_{mix} = -R \sum_{i=1}^{n}(c_i \ln(c_i)) \tag{1}$$

$$\Delta H_{mix} = \sum_{i=1, \, i \neq j}^{n} 4\Delta H_{i,j}^{mix} c_i c_j \tag{2}$$

$$\delta = \sqrt{\sum_{i=1}^{n} c_i \left(1 - \frac{r_i}{\bar{r}}\right)^2} \tag{3}$$

Moreover, Yang and Zhang[6] and King, et al.,[4] calculated dimensionless empirical indexes (Ω and Φ, respectively) from

thermodynamic indicators to predict CCA single-phase stability. Accuracy in the prediction of single-phase stability is improved relative to single parameter criteria by combining multiple thermodynamic values including ΔS_{mix}, ΔH_{mix}, the weighted average melting temperature (T_m), and the enthalpy of the most stable intermetallic binary phase (ΔH_{IM}) into a single term. Single-phase stability is considered likely at values of Ω above 1.1 and Φ above 1.0 where:

$$\Omega = \frac{T_m \Delta S_{mix}}{|\Delta H_{mix}|} \qquad (4)$$

$$\Phi = \left| \frac{\Delta H_{mix} - T_m \Delta S_{mix}}{\Delta H_{IM}} \right| \qquad (5)$$

Further prediction of single-phase stability can be obtained via CALPHAD approaches as well as by combining binary phase diagram analysis with machine learning methods.[2,7]

It has been suggested that CCAs with good mechanical strength[3,8-9] and corrosion resistance benefit from homogenous solid-solution distribution of elements, including key of passivating elements Cr, Al, and Ti.[10-12] Unique combinations and distributions of passivating elements in CCAs, often through elemental synergies not observed in conventional alloys, assist in the formation of stable passive films that prevent further environmental degradation.[11-17]

The use of Al and Ti has been under increased investigation to reduce the density and increase mechanical strength of CCAs.[18-19] Although both elements spontaneously passivate and Ti has been shown to increase corrosion resistance in CCAs,[11,20] face-centered cubic (fcc) alloys reliant on Al and Ti to passivate may have their corrosion resistance decreased by the elements' propensity to form second phases including body-centered cubic (bcc),[1,16,18-19,21-23] B2,[18,23-24] and Heusler (L2$_1$)[1,25-26] phases. Second phase formation driven by Al or Ti, often interacting with Ni,[18-19,23,27] creates both phase boundaries and areas depleted in passivating elements, both of which are potential initiation sites for localized corrosion.[28] Increased second phase volume fractions in the Al$_x$CoCrFeNi system driven by higher Al concentrations lead to decreased pitting potentials and increased passive currents or localized attack in the Al-rich bcc phase.[29]

To improve elemental homogeneity in an fcc matrix, elements conventionally established as austenitic stabilizers may be utilized. Many CCAs, including the first transition metal HEAs developed by Cantor, et al.,[30] utilize Co, Mn, and Ni to stabilize the fcc structure. While Co and Ni often increase alloy cost and density, Mn could potentially function as a cost-effective fcc stabilizer.[31-32] The equimolar introduction of Mn to the AlCrFeNiTi HEA eliminated the formation of a Laves phase and decreased the magnitude of Cr segregation.[27] Higher Mn concentrations in the (FeNi)$_{77-x}$Cr$_{15}$Mn$_x$Al$_4$Ti$_4$ system were computationally modeled to increase the volume fraction of the fcc matrix while changing the stable second phase from the ordered fcc-like L1$_2$ to Laves and bcc phases.[33] Equimolar Mn addition to a mechanically alloyed TiCrFeNi HEA, however, does not remove the Sigma phase that can be eliminated upon Co alloying, suggesting Mn may not be as effective as other austenitic stabilizers.[34] Additionally, it has been proposed that Mn could provide improved mechanical ductility by promoting twinning or transformation induced plasticity to increase CCA ductility.[35-36]

While Mn has been long established as an austenitic stabilizer in stainless steels,[37-38] it is often dismissed in alloy design due to its contributions to poor corrosion resistance. Extensive work in the Fe-Mn-Al system has associated high Mn concentrations with poor corrosion resistance, most prominently attributed to the formation of MnS inclusions.[39] Mn is also detrimental to corrosion resistance due to high elemental dissolution rates.[40-43] Higher Mn concentrations lead to increased levels of pitting and decreased corrosion resistance in the single-phase Fe-Cr-Mn tertiary system, potentially attributable to Mn decreasing the activity of Cr during the passivation process.[44] Similar trends have been observed in single-phase CCAs. Most noticeably, corrosion resistance is improved by removing Mn from equimolar CoCrFeMnNi in sulfate[45] and chloride[46] solutions. The high diffusivity of Mn in CoCrFeMnNi,[47] fast transport rates in Mn oxides, and the instability of Mn-rich passive films[14-15,27,45] may all contribute to the poor corrosion resistance of Mn-containing alloys.

Alternatively, Kukshal, et al.,[48] evaluated Mn additions in the dual phase AlCr$_{1.5}$CuFeNi$_2$Mn$_x$ system up to 13.3 at%, finding increased corrosion resistance with Mn additions that was attributed to improved Cr and Ni distribution in solid solution. Wong, et al.,[49] found that Mn concentrations up to 6.3 at% have an insignificant effect on the corrosion resistance of fcc Al$_{0.3}$CoCrFeNiMn$_x$, with higher Mn concentrations slightly lowering the corrosion potential. Kim and Kim[50] observed an increase in the open-circut potential (OCP) during immersion of a Mn-containing steel that was not observed in the otherwise identical Mn-free composition. Rodriguez, et al.,[51] developed a series of Co-Cr-Fe-Mn-Ni type CCAs with varying Mn concentrations. Corrosion resistance was weakened in alloys with greater than 15 at% Mn, particularly when coupled with decreasing Cr concentrations.

Elements enriched in the passive films are expected to have a negative free energy of formation and kinetically lower electrochemical or chemical dissolution rates during incongruent dissolution of the passivating material, a phenomenon experimentally verified in the bcc Al$_{1.5}$TiVCr CCA by Qiu, et al.[52] Han, et al.,[53] tracked elemental dissolution rates for Ni$_{38}$Fe$_{20}$Cr$_{22}$Mn$_{10}$Co$_{10}$ in a 0.1 M NaCl, pH 4 solution. Potential-dependent Mn dissolution was observed; Mn dissolved incongruently at rates significantly below those of Ni and Fe at 0.1 V$_{SCE}$, whereas it dissolved congruently at 0.0 V$_{SCE}$. Surface enrichment of Mn in the passivating oxides at 0.1 V$_{SCE}$ was verified by x-ray photoelectron spectroscopy (XPS) using 3p core level analysis. At 0.0 V$_{SCE}$, a more corrosion-resistant passive film formation was indicated by the higher oxide resistance obtained by electrochemical impedance spectroscopy (EIS) than that obtained at 0.1 V$_{SCE}$. Better protection was attributed to a lower extent of Mn incorporation in the passive film at this potential. Mn incorporation in oxides could occur by the formation of stable stoichiometric tertiary spinel oxides. FeMn$_2$O$_4$,[54] MnCr$_2$O$_4$,[55] and NiMn$_2$O$_4$[56] stability has been thermodynamically simulated but such ordered spinels have not been experimentally verified to form during aqueous passivation in CoCrFeMnNi[57] or any other Mn-containing CCAs to the authors' best knowledge. The aforementioned findings suggest that corrosion resistance of CCAs is considerably more complex than an inverse proportionality to Mn content. A well-established connection between the alloy nanostructure, microstructure, composition, passive film chemistry, and film protectiveness is currently lacking.

While potential drawbacks of Mn for corrosion resistance are well established, two key gaps in the current understanding

Table 1. *Compositions of Synthesized CCAs in at%*[A]

Alloy	Al (%)	Co (%)	Cr (%)	Fe (%)	Mn (%)	Mo (%)	Ni (%)	Ti (%)
$Al_{0.3}Cr_{0.5}Fe_2Mn_0Mo_{0.15}Ni_{1.5}Ti_{0.3}$	6.3	–	10.5	42.1	**–**	3.2	31.6	6.3
$Al_{0.3}Cr_{0.5}Fe_2Mn_{0.25}Mo_{0.15}Ni_{1.5}Ti_{0.3}$	6.0	–	10.0	40.0	**5.0**	3.0	30.0	6.0
$Al_{0.3}Cr_{0.5}Fe_2Mn_{0.5}Mo_{0.15}Ni_{1.5}Ti_{0.3}$	5.7	–	9.5	38.1	**9.5**	2.9	28.6	5.7
$Al_{0.3}Cr_{0.5}Fe_2Mn_1Mo_{0.15}Ni_{1.5}Ti_{0.3}$	5.2	–	8.7	34.8	**17.4**	2.6	26.1	5.2
CoCrFeMnNi	–	20.0	20.0	20.0	20.0	–	20.0	–
316L	–	–	18.3	66.7	2.1	1.5	11.4	–

[A] Compositions given for 316L indicate an average of the accepted composition range.

introduce potential caveats. First, much of the work on the effect of Mn on corrosion resistance focuses on CCAs with Mn compositions of at least 15 at%, where rapid, preferential dissolution and unprotective Mn oxides can easily harm corrosion resistance in ways that may not occur at lower concentrations. Second, there has been little work on the effect of Mn in Al- and/or Ti-containing multiphase CCAs. The transition metal HEAs CoCrFeMnNi and CoCrFeNi both possess a single-phase fcc microstructure[58] making it difficult to evaluate the tradeoffs between benefits of improved homogeneity from Mn on corrosion distinct from the potential detrimental effect of Mn on oxide protectiveness.

The objective of this work was to examine the effect of Mn in a lightweight alloy with three passivating elements Al, Ti, Cr, one potential oxide dopant element Mo, and a number of austenitic stabilizing elements. The alloys were designed to minimize density and cost while maximizing corrosion resistance and are stipulated to have an fcc matrix. Four CCAs with Mn concentrations ranging from 0 to 17.4 at% were synthesized and characterized to find the optimal Mn concentration to improve corrosion resistance. The role of Mn in the design of lightweight CCAs is investigated by elementally resolved in situ and ex situ techniques.

METHODS

Four CCAs with compositions listed in Table 1 were synthesized by arc-melting from high purity (Cr greater 99.2%, all other metals greater than 99.9%) elements and suction cast in a water-cooled copper hearth under argon atmosphere. Alloys were flipped five times to ensure chemical homogeneity before encapsulation into quartz tubes under argon and a 5 h annealing treatment at 1,070°C followed by a water quench. The compositions and heat treatment were chosen to promote the formation of an fcc matrix while balancing cost, density, and passivating element concentration with machine learning methods discussed elsewhere.[2,7] The $Al_{0.3}Cr_{0.5}Fe_2Mn_x$-$Mo_{0.15}Ni_{1.5}Ti_{0.3}$ system was also modeled with CALPHAD utilizing ThermoCalc[†] 2019b software and the TCHEA3 database for Mn concentrations between 0 and 25 at% to predict the thermodynamically stable phases for each synthesized alloy.[59] Relevant thermodynamic parameters are calculated in Table 2 utilizing previously established atomic radius[60] and enthalpy of mixing[61] values. It was found that the "high" enthalpy criterion, $\Delta S/R$, Ω, and $\varnothing$ where almost met or met while the ∂ criterion

was, expectedly, not achieved. Prediction of an fcc matrix along with a second phases was achieved by machine learning.[2] Samples were cold-mounted in nonconductive epoxy, ground with SiC paper through 1200 grit, and degreased with isopropyl alcohol before electrochemical testing. Diamond polishing suspensions through 0.25 micrometers were used, followed by 0.05-micrometer colloidal silica suspension, to prepare samples for microstructure and surface chemical analysis. The phases in each alloy were identified via x-ray diffraction (XRD) using Cu Kα x-rays (14,68.7 eV) on a PANalytical Empyrean[†] Diffractometer at a scan rate of 0.15 °/s. The samples were characterized through scanning electron microscopy (SEM) using backscattered electron (BSE) imaging on an FEI Quanta 650[†] operating at an accelerating voltage of 15 keV, a spot size of 4, and working distance of approximately 10 mm. The chemical compositions of the samples were evaluated via point scans and mapping with energy dispersive spectroscopy (EDS) analyzed using Oxford Instruments AZtec[†] software. Area fractions of second phase regions were calculated with ImageJ[†] using a brightness threshold to isolate at least 300 precipitates across multiple micrographs per alloy. The calculated area fraction of second phase was taken to be equivalent to the volume fraction of second phase in the material.

Samples, along with equimolar CoCrFeMnNi and commercially procured (North American Steel) Type 316L (UNS S31603[(1)]) stainless steel controls, were potentiodynamically polarized with a Gamry Instrument Reference 600+™[†] potentiostat and a conventional three electrode cell including the CCA sample with an exposed area of 0.785 cm^2 as the working electrode, a platinum mesh counter electrode, and a saturated calomel reference electrode (SCE) relative to which all potentials hereafters are reported. The electrolyte solution was either 0.01 M NaCl, 0.1 M NaCl with the pH unadjusted (approximately 5.75), or 0.1 M NaCl titrated to pH 4 with 1 M HCl. Solutions were dissolved in deionized water and continually bubbled with nitrogen gas throughout testing. Dilute solutions were preferred to observe passivation behavior before interference from localized corrosion. In initial tests, a −1.3 V_{SCE} potential was applied for 600 s to minimize the effect of the air-formed oxide. Cathodic reduction was followed by an upward anodic potential scan from −1.3 V_{SCE} to +0.8 V_{SCE} with a voltage step of 5 mV, continually monitoring the imaginary component of the impedance (Z_{img}) throughout polarization at a frequency of 1 Hz with an AC voltage of 20 mV$_{rms}$, as previously utilized for to evaluate trends in oxide thickness.[14,62] By modeling the oxide film as a constant phase element (CPE) fit to a phase shift (α), resistivity at the interface between the electrolyte and passive film (ρ_δ), applied frequency (f), dielectric constant (κ), vacuum permittivity (ε_o), and exposed area of the working electrode (A),

[†] Trade name.
[(1)] UNS numbers are listed in *Metals & Alloys in the Unified Numbering System*, published by the Society of Automotive Engineers (SAE International) and cosponsored by ASTM International.

Table 2. *Phase Stability Indicators Calculated from the Alloy's Compositions*[(A)]

Alloy	ΔH (kJ/mol)	ΔS/R	δ (%)	Ω	Φ
$Al_{0.3}Cr_{0.5}Fe_2Mo_{0.15}Ni_{1.5}Ti_{0.3}$	−11.07	1.42	8.61	**1.94**	0.929
$Al_{0.3}Cr_{0.5}Fe_2Mn_{0.25}Mo_{0.15}Ni_{1.5}Ti_{0.3}$	−10.74	**1.55**	8.42	**2.16**	0.968
$Al_{0.3}Cr_{0.5}Fe_2Mn_{0.5}Mo_{0.15}Ni_{1.5}Ti_{0.3}$	−10.39	**1.60**	8.25	**2.29**	0.976
$Al_{0.3}Cr_{0.5}Fe_2Mn_1Mo_{0.15}Ni_{1.5}Ti_{0.3}$	−9.77	**1.64**	7.90	**2.45**	0.963
CoCrFeMnNi	−4.16	**1.61**	**3.90**	**5.79**	**3.533**
316L	−1.85	0.97	**3.96**	**8.22**	**2.130**

[(A)] Bolded terms indicate values associated with single-phase stability in CCAs.

Z_{img} may be modeled as directly proportional to the oxide thickness (l_{ox}).[(2) 63-64]

$$|Z_{img}| = \frac{l_{ox}\rho_\delta^{1-\alpha} \sin(\frac{\alpha\pi}{2})(1 + 2.88(1-\alpha)^{2.375})}{2\pi f\kappa\varepsilon_o A} \qquad (6)$$

Finally, the sample was polarized in the reverse direction (+0.8 V_{SCE} to −1.3 V_{SCE}) with otherwise identical methods. Pitting potentials are defined at the potential where the current density first reaches 10^{-5} A/cm^2 and zero current potentials are defined where the net applied current density is equal to zero.

To characterize the oxide films spontaneously formed in air and modified by OCP exposure, a second procedure was utilized. Directly after grinding a new surface (approximately 10 min at room temperature, 62.4% relative humidity), OCP was monitored for 1,800 s in 0.01 M NaCl. Potentiostatic EIS was conducted at the potential of the final OCP measurement at a frequency range from 100 kHz to 1 mHz with 5 points/decade and an AC voltage of 20 mV$_{rms}$. The sample was polarized with a potential scan from 0.1 V below OCP to +0.8 V_{SCE} with the same continual impedance monitoring methodology utilized during previous polarization experiments followed by a reversed downward scan (+0.8 V_{SCE} to −1.3 V_{SCE}).

To characterize the passive oxide growth, a potential of −1.3 V_{SCE} was applied to each CCA for 600 s before applying a constant potential of −0.25 V_{SCE} for 40 ks, verified to be within the passive range of all tested alloys via potentiodynamic polarization. The Z_{img} was continually characterized every 6 s at a frequency of 1 Hz and an AC voltage of 20 mV$_{rms}$ to monitor oxide growth during the potentiostatic hold. The potentiostatic EIS described above was carried out at −0.25 V_{SCE} to characterize the surface after the potentiostatic hold. EIS spectra were fit to a simplified Randles' circuit model containing a CPE with Gamry Echem Analyst[†] software to obtain the polarization resistance of the oxide film.

To examine the effects of a longer time of corrosion, 1 cm diameter buttons with a thickness of approximately 0.25 cm were measured for mass to 0.01 mg precision and fully immersed for 25 d in 0.1 M NaCl. Corrosion products were rinsed with nitric acid under ASTM Standard G1 C.7.4[65] and the sample was remeasured for mass. The change in mass was normalized to exposed surface area to calculate the mass loss rate and to a weighted elemental average density to obtain the penetration

rate. An 1,800 s OCP measurement followed by the EIS spectrum described above at each alloy's respective OCP was collected in a separate flat cell both directly prior to and following immersion of $Al_{0.3}Cr_{0.5}Fe_2Mn_0Mo_{0.15}Ni_{1.5}Ti_{0.3}$ and $Al_{0.3}Cr_{0.5}Fe_2Mn_{0.25}Mo_{0.15}Ni_{1.5}Ti_{0.3}$.

Atomic emission spectroelectrochemistry (AESEC) was used to monitor individual elemental dissolution rates alongside electron current density. Dissolved elements were transferred through a flow cell to a Horiba Jobin Yvon Ultima 2C[†] inductively coupled plasma atomic emission spectrometer (ICP-AES). The dissolution rates of each alloying element in $Al_{0.3}Cr_{0.5}Fe_2Mn_0Mo_{0.15}Ni_{1.5}Ti_{0.3}$, $Al_{0.3}Cr_{0.5}Fe_2Mn_{0.25}Mo_{0.15}Ni_{1.5}Ti_{0.3}$, and $Al_{0.3}Cr_{0.5}Fe_2Mn_1Mo_{0.15}Ni_{1.5}Ti_{0.3}$ alloys were monitored by emission intensity at a characteristic wavelength of each element with a polychromator at a 0.5 m focal length. A monochromator was used to have an improved signal resolution of Mo or Cr. Elemental dissolution rates (v_M) were converted to an equivalent elemental current density (j_M) with Faraday's law, providing a comparable basis to electron current density (j_e). A theoretical basis for AESEC and comprehensive methodology may be found elsewhere.[66] AESEC experiments were performed in a 0.1 M NaCl pH 4 solution to increase the dissolution rate to an observable level. Dissolution rates were monitored during potentiodynamic polarization following a 600 s exposure to open-circuit corrosion and an application of a −1.3 V_{SCE} potential for 600 s. Potentials were swept from −1.3 V_{SCE} to +0.8 V_{SCE} with a scan rate of 0.5 mV/s. Dissolution rates were monitored during a 600 s exposure to open-circuit corrosion and during a directly following 4 ks potentiostatic hold at −0.2 V_{SCE} (bypassing any cathodic reduction). The test time was decreased relative to electrochemical tests to ensure plasma stability.

Chemical compositions of passive films grown on $Al_{0.3}Cr_{0.5}Fe_2Mn_{0.25}Mo_{0.15}Ni_{1.5}Ti_{0.3}$ and $Al_{0.3}Cr_{0.5}Fe_2Mn_1Mo_{0.15}Ni_{1.5}Ti_{0.3}$ during the 40 ks potentiostatic hold were characterized with XPS spectra acquired with Al Kα X-rays (1,468.7 eV) at a 26 eV pass energy, 45° take off angle, and with a 100 μm spot size in a PHI VersaProbe III[†] system. High-resolution spectra over the Al 2p, Cr 2p$_{3/2}$, Fe 2p$_{1/2}$, Mn 2p$_{1/2}$, Mo 3d, Ni 2p$_{3/2}$, and Ti 2p$_{3/2}$ core series were shifted utilizing C 1s = 284.8 eV and deconvoluted with Shirley background subtractions, Doniach-Sunjic peaks for metallic features, and Voigt functions for oxidized features with KOLXPD™[†] analysis software. Metal and oxidized peaks were identified by considering position, shape, and multiplet splitting identified from reference spectra of Al,[67] Ti,[68] Mo,[69] the first-row transition[70] metals, and their oxidized compounds. In the case of Fe and Mn, where Ni Auger peaks overlap the 2p$_{3/2}$ series,[71] a constant binding energy shift for each compound relative to the reference 2p$_{3/2}$ spectra was assumed. Cation fractions were normalized with relative

---

[(2)] Although oxide thicknesses could be quantified with a dielectric constant and resistivity estimated from XPS-based surface analysis, such assumptions were not made to characterize the film during polarization due to the changing composition of the oxide film. Therefore, the trends in the Z_{img} measured during polarization and/or potentiostatic holds should be regarded as qualitative descriptions of the oxide film thickness.

sensitivity factors obtained from Phi Multipak[†] software. The overlap between the Al 2p series and Cr 3s series was accounted for by fixing the magnitude of Cr 3s signal based on the intensity obtained in the Cr 2p 3/2 region normalized by relative sensitivity factors. Cation fractions were evaluated as the proportion of each elements normalized intensities for all oxidized states summed relative to that of all elements' oxidized state intensities. The cation enrichment (or depletion) factors f_A for each individual element "A" were calculated from the surface composition (X^S), in this case, the oxide cation fraction obtained by XPS, relative to the sum of the bulk compositional fraction all other constituent elements (X_j) normalized to their bulk alloy compositions (X^b):[72]

$$f_A = \frac{\frac{X_A^S}{X_A^S + \Sigma_j X_J^S}}{\frac{X_A^b}{X_A^b + \Sigma_j X_J^b}} \qquad (7)$$

RESULTS

3.1 | Microstructural Characterization of Compositionally Complex Alloys

XRD suggests an fcc matrix indexable to a lattice parameter of 3.63 Å for alloys with all Mn concentrations, as shown in Figure 1. Second phase regions of either bcc or ordered bcc-type (B2/L2$_1$) are visible in the XRD data for Al$_{0.3}$Cr$_{0.5}$Fe$_2$Mn$_0$Mo$_{0.15}$Ni$_{1.5}$Ti$_{0.3}$ and Al$_{0.3}$Cr$_{0.5}$Fe$_2$Mn$_{0.25}$Mo$_{0.15}$Ni$_{1.5}$Ti$_{0.3}$, the two alloys with the lowest Mn concentration, however, noise in XRD data prevents accurate phase identification from additional peaks. The CALPHAD modeling seen in Figure 2 does not accurately identify the phase structure, suggesting the synthesized alloys would form a single fcc phase, however, it does indicate a broad fcc-L1$_2$ phase region above 1,290°C which broadens slightly with Mn content from 0 to 25 at%. Below this temperature many phases are formed including L2$_1$, Mu, Laves, and Sigma depending on the exact Mn content. Second phase regions on the order of single microns with similar spacing distributions are visible in the BSE micrographs for all four CCAs (Figure 3). There is a nonmonotonic trend of second phase area fraction and Mn concentration.
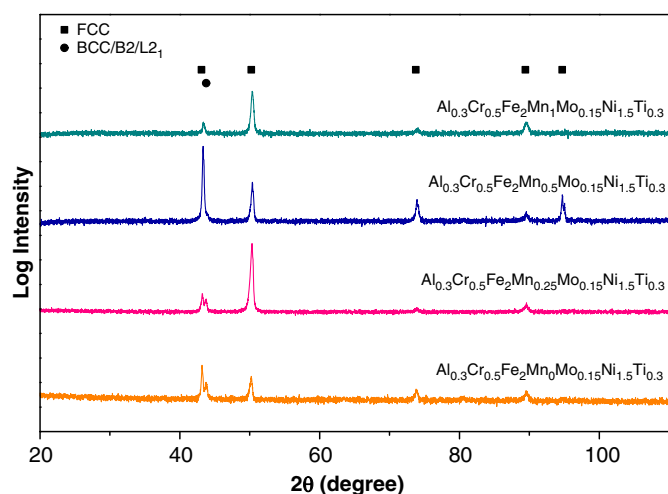
EDS mapping (Figure 4) and point scans (Table 3) suggest Fe, Cr, and Mo enrichment in the matrix and Al, Ti, and Ni enrichment in the second phase regions relative to the bulk metal concentrations. Fe and Ni have the highest concentrations in the matrix and second phase, respectively. Mn has a similar composition in both regions in all CCAs. The differences in matrix and second phase particle compositions for each element generally have the highest magnitude for Al$_{0.3}$Cr$_{0.5}$Fe$_2$Mn$_0$Mo$_{0.15}$Ni$_{1.5}$Ti$_{0.3}$. The other CCAs have similar composition ratios between the phases for most elements regardless of Mn concentration. Ti- and N-rich or Al-, Ti-, and O-rich impurities from contamination during synthesis are also present in low quantities throughout the microstructures.

3.2 | AC and DC Electrochemical Corrosion Results on Compositionally Complex Alloys

Figure 5(a) reports anodic and cathodic polarization curves in 0.01 M NaCl in E-log(i) format after applying a −1.3 V$_{SCE}$ potential for 600 s to minimize the effect of the native oxide for Al$_{0.3}$Cr$_{0.5}$Fe$_2$Mn$_0$Mo$_{0.15}$Ni$_{1.5}$Ti$_{0.3}$, Al$_{0.3}$Cr$_{0.5}$Fe$_2$Mn$_{0.25}$Mo$_{0.15}$Ni$_{1.5}$Ti$_{0.3}$, Al$_{0.3}$Cr$_{0.5}$Fe$_2$Mn$_{0.5}$Mo$_{0.15}$Ni$_{1.5}$Ti$_{0.3}$, and Al$_{0.3}$Cr$_{0.5}$Fe$_2$Mn$_1$Mo$_{0.15}$Ni$_{1.5}$Ti$_{0.3}$. The dilute solution is utilized to observe the passive range prior to breakdown. The E-log(i) plot for the experimental CCAs is compared to CoCrFeMnNi and 316L stainless steel. The E-log(i) data shows the improved corrosion resistance of Al$_{0.3}$Cr$_{0.5}$Fe$_2$Mn$_{0.25}$Mo$_{0.15}$Ni$_{1.5}$Ti$_{0.3}$ relative to CCAs with both higher and lower Mn contents, evidenced by the lower current density of Al$_{0.3}$Cr$_{0.5}$Fe$_2$Mn$_{0.25}$Mo$_{0.15}$Ni$_{1.5}$Ti$_{0.3}$ in the passive potential domain. The pitting potential of Al$_{0.3}$Cr$_{0.5}$Fe$_2$Mn$_{0.25}$Mo$_{0.15}$Ni$_{1.5}$Ti$_{0.3}$ is comparable to that of 316L and is higher than all other tested CCAs. Current spikes before a sharp increase suggest metastable pitting and passive film breakdown. Overall, the CCAs show generally higher passive current densities than 316L. Both increased current densities in the passive potential domain and more negative zero current potentials of the CCAs relative to 316L suggest that the passive films are less protective on the CCAs thus the alloys are less polarizable. CoCrFeMnNi, which has a significantly higher Mn concentration to 316L, has inferior corrosion resistance despite greater Cr concentration.

In situ Z$_{img}$ measurements (Figure 5[b]) indicate multiple peaks and generally increase in magnitude throughout the upward potential sweep. The parameter increases at potential below −1.0 V$_{SCE}$ indicative of less noble oxides forming early in the scan. From −0.5 V$_{SCE}$ to +0.5 V$_{SCE}$ the change in Z$_{img}$ is linear suggesting oxide thickness is directly proportional to applied potential. This parameter decreases near the pitting potentials with varying degrees of abruptness. Sharp decreases in Z$_{img}$ may indicate the passive film breakdown coinciding with sharp current spikes in current in the E-log(i) plots. It should be noted that the Z$_{img}$ of Al$_{0.3}$Cr$_{0.5}$Fe$_2$Mn$_{0.25}$Mo$_{0.15}$Ni$_{1.5}$Ti$_{0.3}$ is greater than all other CCAs, CoCrFeMnNi, and 316L at most potentials, which may indicate the formation of a relatively thicker and/or more corrosion-resistant passive film with different composition and dielectric constant.

The corrosion products formed during electrochemical measurement are generally translucent and either gray or colorless. Pitting is the most prevalent form of corrosion damage visible and is suggested to be the primary cause of passive film breakdown. Significant crevice corrosion was not visible at the sample/epoxy interface. Pitting occurs over the entire surface of the sample, however, a cluster of large pits is frequently seen in the center of the sample.

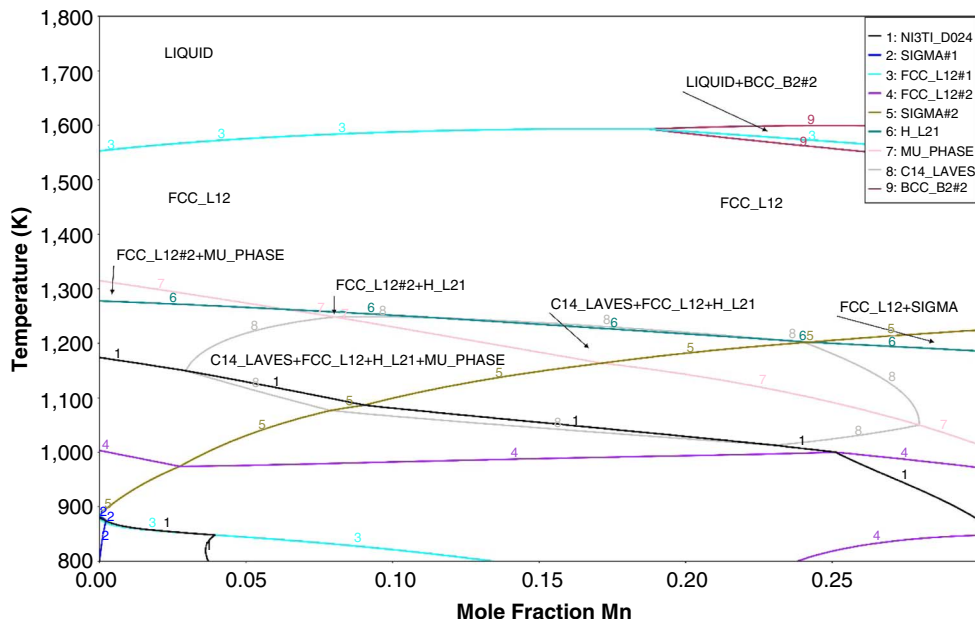**FIGURE 1.** *XRD spectra for synthesized CCAs indexed to fcc and bcc/B2/L2$_1$ phases.*

FIGURE 2. $Al_{0.3}Cr_{0.5}Fe_2Mn_xMo_{0.15}Ni_{1.5}Ti_{0.3}$ system modeled with CALPHAD from Thermocalc TCHEA3 database.
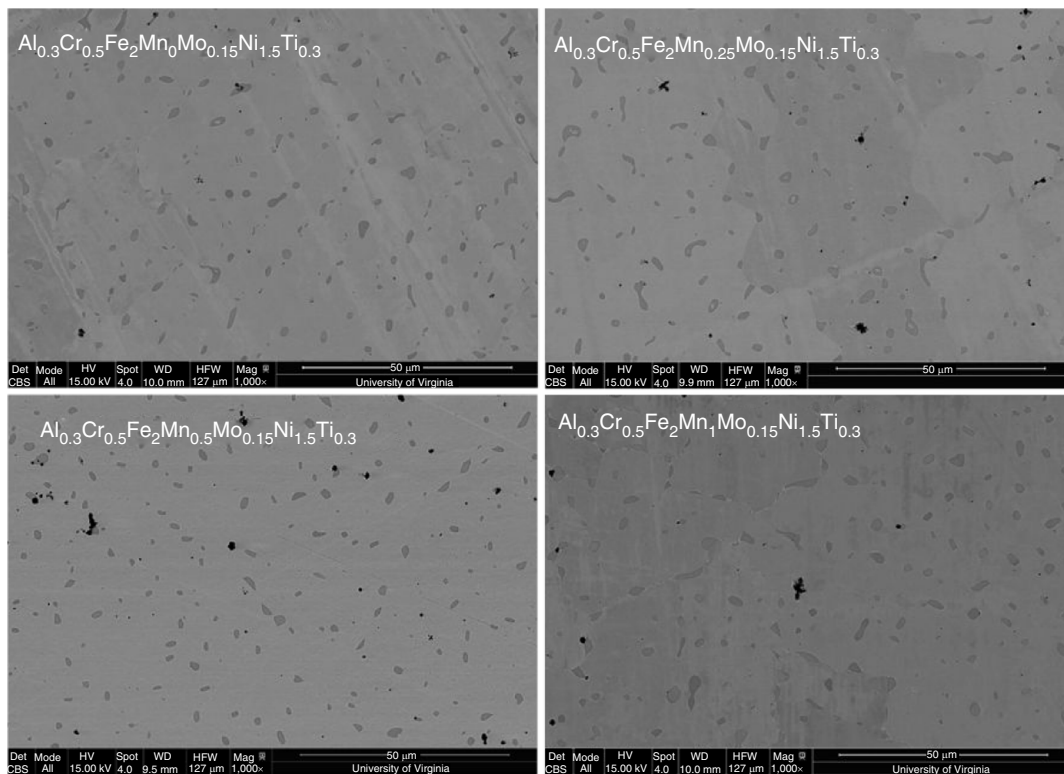

FIGURE 3. BSE images of CCA microstructures.

The cyclic polarization scans (Figure 6) show a similar repassivation potential to 316L, defined where current densities return to levels lower than the passive current, during the downward scan of $Al_{0.3}Cr_{0.5}Fe_2Mn_{0.25}Mo_{0.15}Ni_{1.5}Ti_{0.3}$ relative to 316L. The lower current densities in the downward scan and higher repassivation potential suggest improved repassivation in $Al_{0.3}Cr_{0.5}Fe_2Mn_{0.25}Mo_{0.15}Ni_{1.5}Ti_{0.3}$ relative to 316L.

$Al_{0.3}Cr_{0.5}Fe_2Mn_{0.25}Mo_{0.15}Ni_{1.5}Ti_{0.3}$ has a higher repassivation potential than all other CCAs, further justifying it as the most corrosion resistant CCA evaluated. Similar to $Al_{0.3}Cr_{0.5}Fe_2Mn_{0.25}Mo_{0.15}Ni_{1.5}Ti_{0.3}$ and 316 L, a positive hysteresis is present in the downward polarization scans of all other tested alloys (not shown). The pitting, repassivation, and zero current potentials determined from polarization in 0.01 M NaCl are given
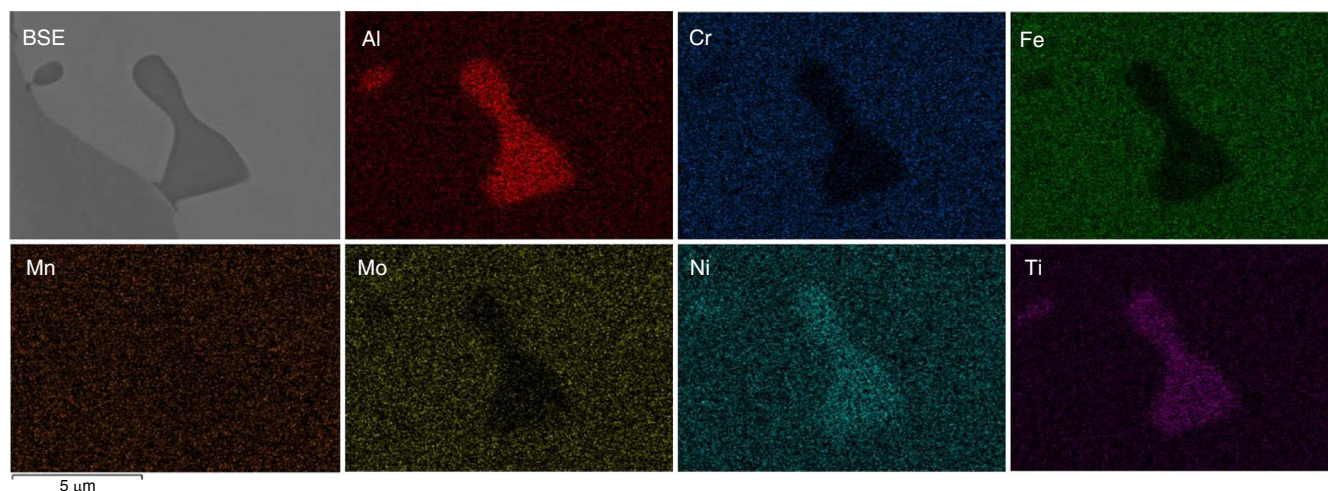
FIGURE 4. *A representative second phase containing region identified with BSE imaging and EDS mapping demonstrating elemental segregation in $Al_{0.3}Cr_{0.5}Fe_2Mn_{0.25}Mo_{0.15}Ni_{1.5}Ti_{0.3}$.*

Table 3. *Elemental Fractions Obtained with EDS Point Scans in the Matrix and Second Phase of the Synthesized CCAs[(A)]*

Phase	Al	Cr	Fe	Mn	Mo	Ni	Ti	Area Fraction (%)
$Al_{0.3}Cr_{0.5}Fe_2Mn_0Mo_{0.15}Ni_{1.5}Ti_{0.3}$								
Matrix	3.73	11.58	44.67	–	3.24	30.65	6.13	96.04
2nd Phase	15.28	2.50	13.95	–	0.51	47.26	20.49	3.96
$Al_{0.3}Cr_{0.5}Fe_2Mn_{0.25}Mo_{0.15}Ni_{1.5}Ti_{0.3}$								
Matrix	3.70	11.02	42.49	5.24	3.12	28.78	5.63	95.67
2nd Phase	14.31	3.54	17.13	4.24	0.87	44.08	15.83	4.33
$Al_{0.3}Cr_{0.5}Fe_2Mn_{0.5}Mo_{0.15}Ni_{1.5}Ti_{0.3}$								
Matrix	5.22	9.95	39.85	9.37	2.66	27.78	5.17	96.70
2nd Phase	17.10	3.21	18.20	8.44	0.69	40.97	11.40	3.30
$Al_{0.3}Cr_{0.5}Fe_2Mn_1Mo_{0.15}Ni_{1.5}Ti_{0.3}$								
Matrix	4.39	9.31	35.78	18.71	1.97	25.16	4.69	94.37
2nd Phase	15.27	2.88	14.96	15.73	0.58	39.39	11.19	5.63

[(A)] Area fraction referrers to the cross-sectional second phase area fraction calculated through microstructural analysis with ImageJ.

in Figure 7 and Table 4, which enable comparison of the corrosion resistance between CCAs as a function of Mn content. The pitting potentials decrease with increased Mn content beyond 5 at%, which suggest poor corrosion resistance for the high Mn CCAs. Trends in the zero current potential are not as prominent, partially attributable to the inconsistency of $Al_{0.3}Cr_{0.5}Fe_2Mn_{0.5}Mo_{0.15}Ni_{1.5}Ti_{0.3}$ results. Interestingly, both the highest and lowest Mn concentrations show the lowest pitting, zero current, and repassivation potentials in 0.01 M NaCl, suggesting the presence of an optimal Mn concentration between the extremes.

Electrochemical response in a more concentrated Cl⁻ environments was evaluated by potentiodynamic polarization in 0.1 M NaCl (Figure 8). Similar E-log(i) trends and effects of Mn are observed as those obtained from polarization in 0.01 M NaCl (Figure 7). The increase in Cl⁻ concentration decreases pitting potential from those obtained in 0.01 M NaCl. A gray or gold corrosion product slightly more opaque than when formed

0.01 M NaCl is visible after polarization. $Al_{0.3}Cr_{0.5}Fe_2Mn_{0.25}Mo_{0.15}Ni_{1.5}Ti_{0.3}$ has the highest pitting potential of all alloys, similar to the results observed in 0.01 M NaCl. At low potentials, however, $Al_{0.3}Cr_{0.5}Fe_2Mn_0Mo_{0.15}Ni_{1.5}Ti_{0.3}$ and CoCrFeMnNi both have lower current densities and higher Z_{img} values than $Al_{0.3}Cr_{0.5}Fe_2Mn_{0.25}Mo_{0.15}Ni_{1.5}Ti_{0.3}$. The correlation between passive current density and Mn content is more prominent in 0.1 M NaCl than in 0.01 M NaCl. In 0.1 M NaCl pH 4 solution, similar qualitative trends were observed (Figure 9). Passive film breakdown occurred in the form of pitting with limited crevice corrosion. The three CCAs with Mn concentrations below 10 at% showed similar breakdown potentials, while a decrease with higher Mn concentration, confirming trends established in neutral solutions. The Z_{img} component during polarization was significantly lower across most potentials for the oxide film grown in pH 4 than those grown in neutral solutions or formed during exposure to air. It should be noted that the highest Mn containing alloys all had a low Z_{img} at 0 V_{SCE}.
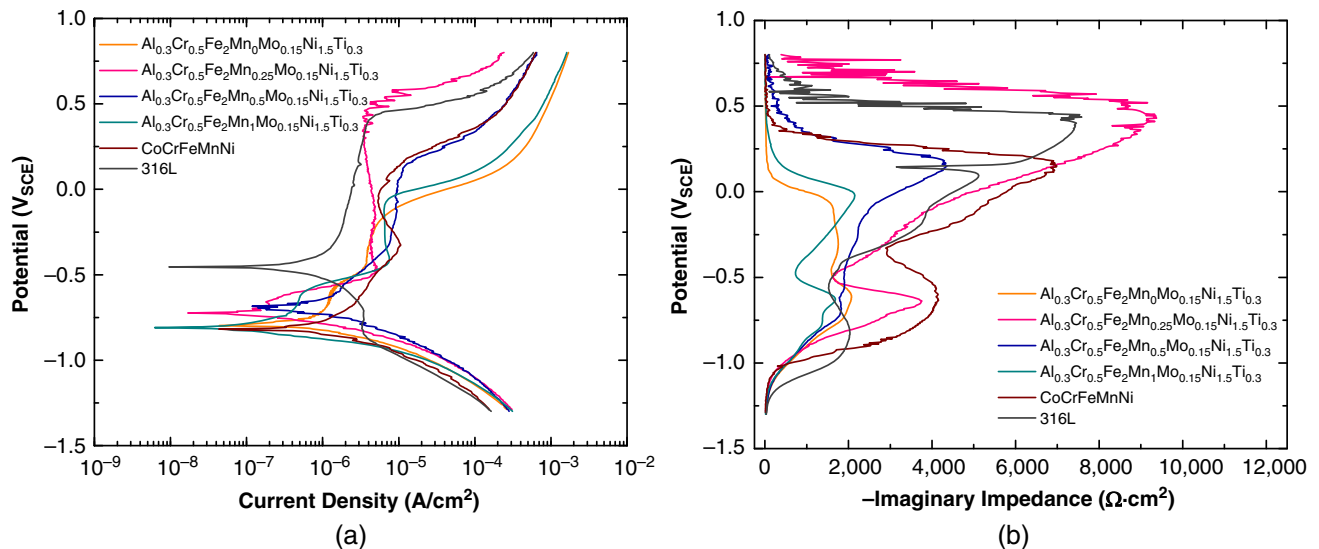
FIGURE 5. *(a) E-log(i) curves and (b) in situ imaginary impedance measurements obtained during upward polarization of CCAs in 0.01 M NaCl after a 600 s application of a −1.3 V_{SCE} potential compared to CoCrFeMnNi and 316L.*

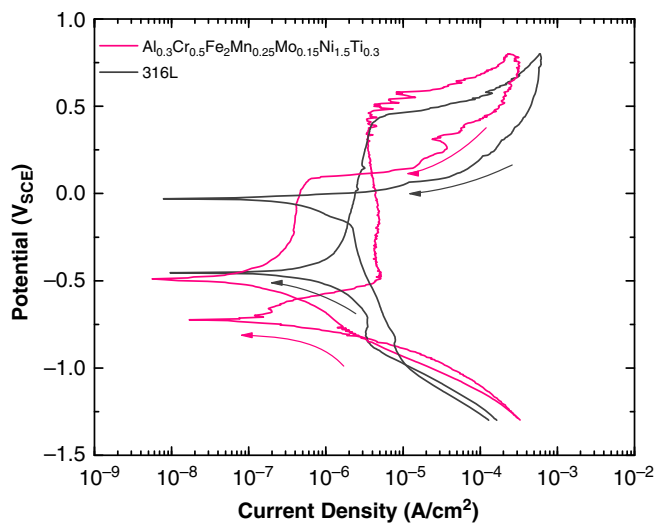**FIGURE 6.** *E-log(i) curves of cyclic polarization of $Al_{0.3}Cr_{0.5}Fe_2Mn_{0.25}Mo_{0.15}Ni_{1.5}Ti_{0.3}$ and 316L in 0.01 M NaCl. Scan direction is indicated by arrows.*
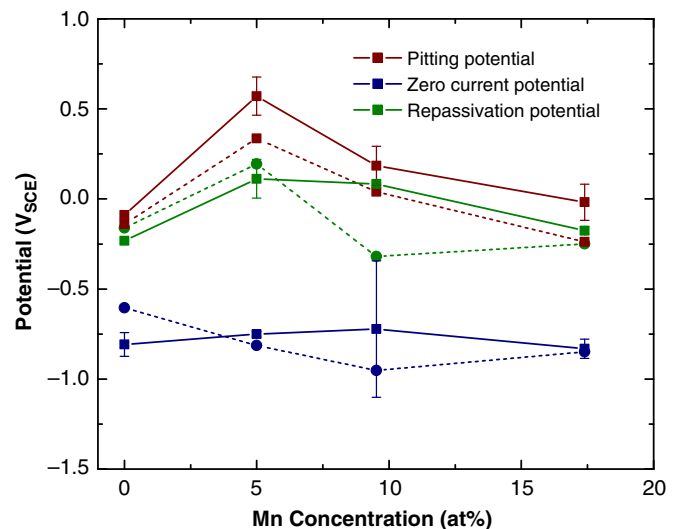

FIGURE 7. *Pitting, zero current, and repassivation potentials measured during polarization of the CCAs in 0.01 M NaCl. Error bars correspond to one standard deviation from the indicated potentials. The pitting, zero current, and repassivation potentials in 0.1 M NaCl indicated by dashed lines are provided for comparative purposes.*

Figure 10 shows polarization curves in 0.01 M NaCl intended to characterize the corrosion resistance of natural oxide films formed by air exposure directly after grinding. Polarization curves of the air-formed oxides obtained after exposure to open-circuit corrosion for 1,800 s show similar trends as those after reduction at −1.3 V_{SCE}. $Al_{0.3}Cr_{0.5}Fe_2Mn_{0.25}Mo_{0.15}Ni_{1.5}Ti_{0.3}$ shows a higher pitting potential that is over 0.35 V above that of 316L and is higher than all other CCAs. The Z_{img} of $Al_{0.3}Cr_{0.5}Fe_2Mn_0Mo_{0.15}Ni_{1.5}Ti_{0.3}$, $Al_{0.3}Cr_{0.5}Fe_2Mn_1Mo_{0.15}Ni_{1.5}Ti_{0.3}$, and CoCrFeMnNi continuously decreases with increasing potential, suggesting oxide instability in the solution, whereas it sharply decreases at the breakdown potentials in $Al_{0.3}Cr_{0.5}Fe_2Mn_{0.25}Mo_{0.15}Ni_{1.5}Ti_{0.3}$ and 316L. Weakening and/ or partial breakdown of the air-formed oxide may occur on some alloys during initial exposure to the solution with no applied potential, as OCP decreases during the 1,800 s measurement prior to polarization for $Al_{0.3}Cr_{0.5}Fe_2Mn_0Mo_{0.15}Ni_{1.5}Ti_{0.3}$,

$Al_{0.3}Cr_{0.5}Fe_2Mn_1Mo_{0.15}Ni_{1.5}Ti_{0.3}$, and CoCrFeMnNi. In contrast, OCP increases for $Al_{0.3}Cr_{0.5}Fe_2Mn_{0.25}Mo_{0.15}Ni_{1.5}Ti_{0.3}$, $Al_{0.3}Cr_{0.5}Fe_2Mn_{0.5}Mo_{0.15}Ni_{1.5}Ti_{0.3}$, and 316L (not shown).

The effect of Mn on pitting potential is more obvious in air-formed oxides than those formed after a reduction treatment in the same solution. Additionally, both the zero current and repassivation potentials of $Al_{0.3}Cr_{0.5}Fe_2Mn_{0.25}Mo_{0.15}Ni_{1.5}Ti_{0.3}$ are greater than the other CCAs, with both potentials decreasing in CCAs with increased Mn content beyond 5 at% (Figure 11). Figure 12 shows the maximum Z_{img} measured in situ during polarization. In both the oxide formed after a cathodic treatment and the air formed oxide, $Al_{0.3}Cr_{0.5}Fe_2Mn_{0.25}Mo_{0.15}Ni_{1.5}Ti_{0.3}$ has the highest maximum Z_{img} with the magnitude decreasing with increased Mn concentration.

Table 4. *Pitting (E_{pit}), Repassivation (E_{rep}), and Zero Current ($E_{i=0}$) Potentials of the CCAs Polarized in 0.01 M NaCl Both Directly After a 600s Cathodic Reduction at −1.3 V_{SCE} and Bypassing the Treatment to Characterize the Air-Formed Oxide*[A]

Alloy	Post-Reduction Solution Formed Oxide				Air-Formed Oxide		
	E_{pit} (V_{SCE})	E_{rep} (V_{SCE})	$E_{i=0}$ (V_{SCE})	i(E = −0.25 V_{SCE}) (A/cm^2)	E_{pit} (V_{SCE})	E_{rep} (V_{SCE})	$E_{i=0}$ (V_{SCE})
$Al_{0.3}Cr_{0.5}Fe_2Mn_0Mo_{0.15}Ni_{1.5}Ti_{0.3}$	−0.188	−0.227	−0.797	4.69×10^{-6}	N/A	−0.149	−0.253
$Al_{0.3}Cr_{0.5}Fe_2Mn_{0.25}Mo_{0.15}Ni_{1.5}Ti_{0.3}$	0.464	0.117	−0.720	4.51×10^{-6}	0.749	0.300	−0.166
$Al_{0.3}Cr_{0.5}Fe_2Mn_{0.5}Mo_{0.15}Ni_{1.5}Ti_{0.3}$	0.276	0.076	−0.354	2.90×10^{-6}	0.453	0.151	−0.196
$Al_{0.3}Cr_{0.5}Fe_2Mn_1Mo_{0.15}Ni_{1.5}Ti_{0.3}$	−0.049	−0.172	−0.802	6.68×10^{-6}	N/A	−0.290	−0.181
CoCrFeMnNi	0.069	−0.125	−0.819	8.45×10^{-6}	0.263	−0.292	−0.299
316L	0.403	0.004	−0.455	1.71×10^{-6}	0.396	0.060	−0.134

[A] The indicated current densities, i(E = −0.25 V_{SCE}), were obtained within the passive range during polarization.
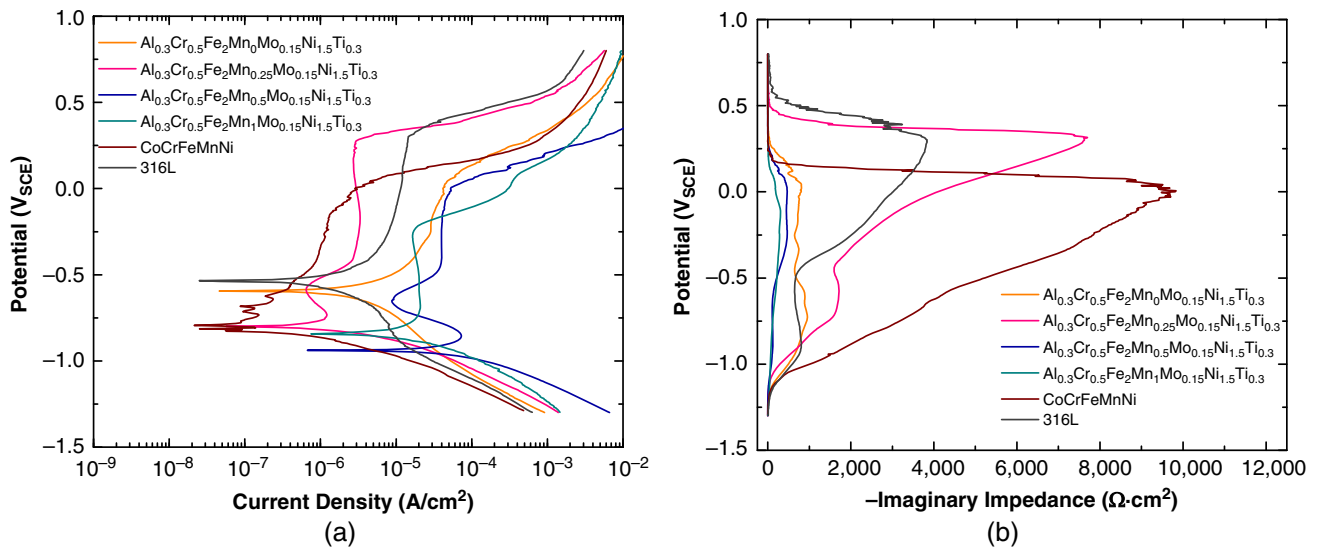

FIGURE 8. *(a) E-log(i) curves and (b) in situ imaginary impedance measurements obtained during upward polarization of CCAs in 0.1 M NaCl after a 600 s application of a −1.3 V_{SCE} potential.*
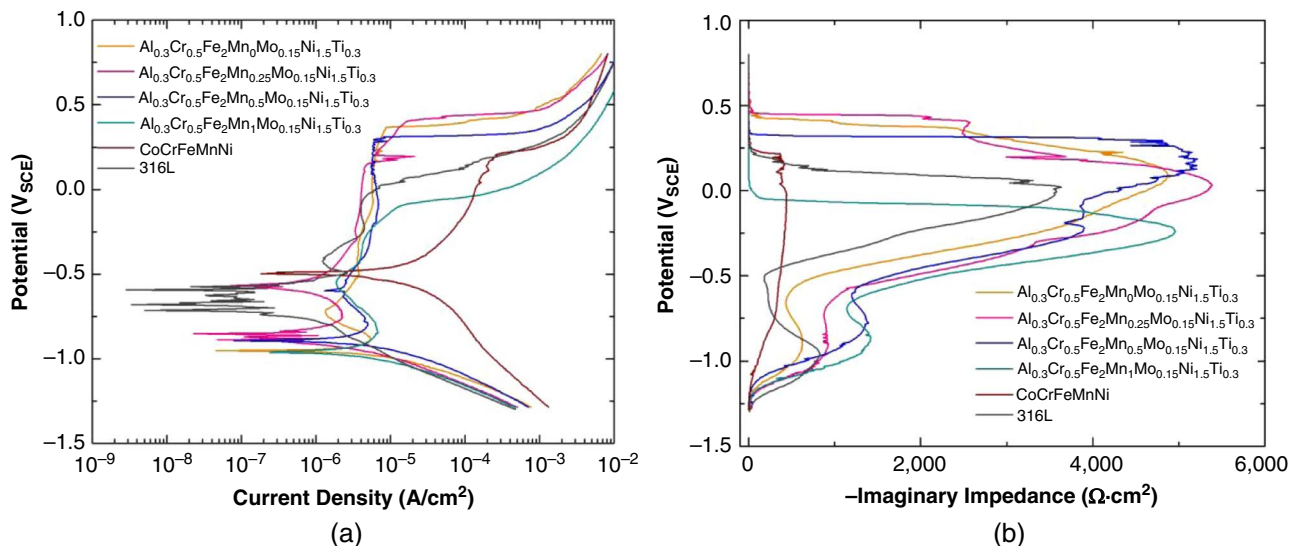

FIGURE 9. *(a) E-log(i) curves and (b) in situ imaginary impedance measurements obtained during upward polarization of CCAs in 0.1 M NaCl pH 4 after a 600 s application of a −1.3 V_{SCE} potential.*
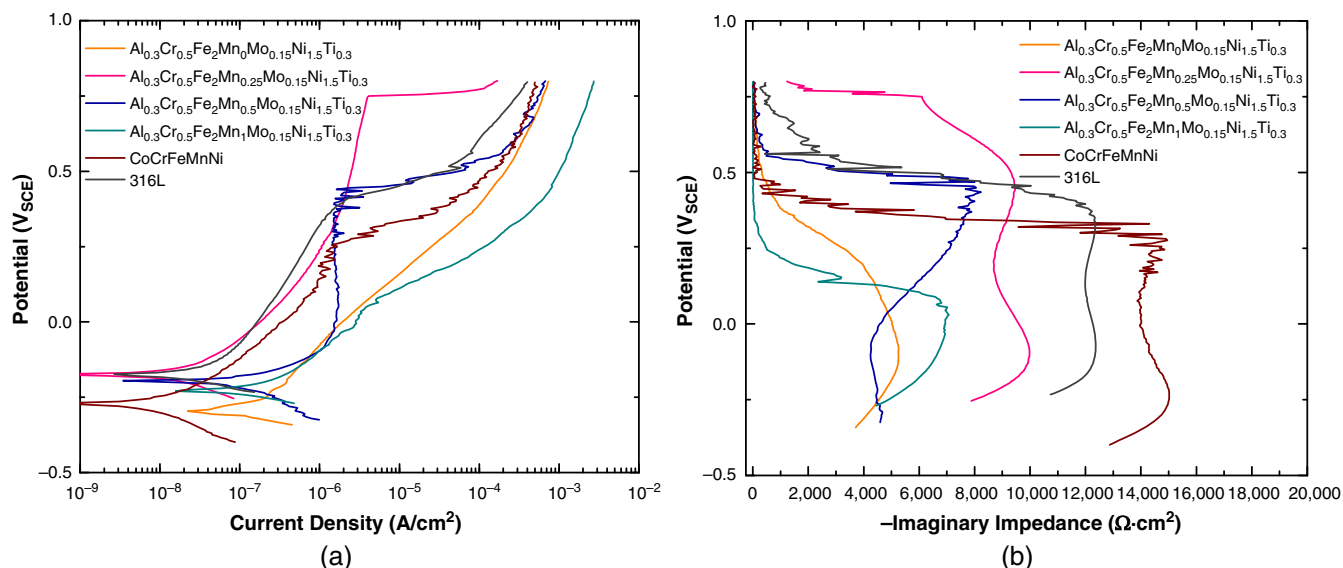
FIGURE 10. *(a) E-log(i) polarization curves and (b) in situ impedance measurements obtained during polarization in 0.01 M NaCl directly after open-circuit monitoring of the air-formed oxide.*
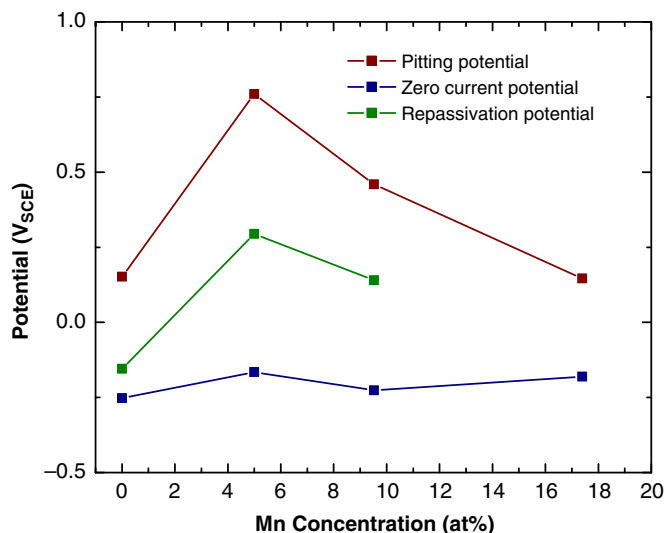

FIGURE 11. *Pitting, zero current, and repassivation potentials measured during polarization in 0.01 M NaCl directly after open-circuit monitoring of the air-formed oxide. A repassivation potential could not be defined for $Al_{0.3}Cr_{0.5}Fe_2Mn_1Mo_{0.15}Ni_{1.5}Ti_{0.3}$ as the downward scan current density never reestablished as lower than the upward scan current density for any given potential.*

Figure 13 reports the current density (i) (Figure 13[a]) and Z_{img} (Figure 13[b]) during oxide growth with an applied potential of -0.25 V_{SCE} for 40 ks in 0.01 M NaCl. As the potential is applied directly after a -1.3 V_{SCE} treatment, the oxide is assumed to be passivated on a reduced metal surface. During the potentiostatic measurement, decreases in current density between 10 s and 1,000 s are indicative of a growing passive film. Discerning oxide growth before 10 s is difficult as the time range approaches the impedance recording period of 6 s per measurement. In $Al_{0.3}Cr_{0.5}Fe_2Mn_{0.25}Mo_{0.15}Ni_{1.5}Ti_{0.3}$ and $Al_{0.3}Cr_{0.5}Fe_2Mn_1Mo_{0.15}Ni_{1.5}Ti_{0.3}$, the reaction undergoes a transition from cathodic to anodic, indicated by the sharp drop on the log i vs. log t plot as i approaches zero. At the transition,

the current direction changes from positive to negative. Z_{img} increases over the same time and then levels off suggesting a limiting film thickness.

Potentiostatic EIS was performed for each alloy at the conclusion of the 40 ks growth period and fit to a Randles' circuit model (Figure 14). Table 5 shows the polarization resistances and phase shift proposed by circuit fitting. 1 Hz is within the linear capacitive region of the Bode plot for all alloys, validating the selection of the frequency for single frequency EIS characterization. $Al_{0.3}Cr_{0.5}Fe_2Mn_{0.25}Mo_{0.15}Ni_{1.5}Ti_{0.3}$ has the highest polarization resistance, suggesting that this alloy would show the highest corrosion resistance. However, the other CCAs show higher impedance moduli than $Al_{0.3}Cr_{0.5}Fe_2Mn_{0.25}Mo_{0.15}Ni_{1.5}Ti_{0.3}$ in the high-frequency domain, including 1 Hz which is consistent with the higher impedance moduli seen approaching 40 ks during single frequency EIS (Figure 13[a]). $Al_{0.3}Cr_{0.5}Fe_2Mn_0Mo_{0.15}Ni_{1.5}Ti_{0.3}$, $Al_{0.3}Cr_{0.5}Fe_2Mn_{0.5}Mo_{0.15}Ni_{1.5}Ti_{0.3}$, and $Al_{0.3}Cr_{0.5}Fe_2Mn_1Mo_{0.15}Ni_{1.5}Ti_{0.3}$ all have lower polarization resistances and generally lower phase angles compared to $Al_{0.3}Cr_{0.5}Fe_2Mn_{0.25}Mo_{0.15}Ni_{1.5}Ti_{0.3}$. Although high α terms indicate the passive films approach capacitor behavior, deviation from pure capacitive behavior is present. There is no strong correlation between α and Mn content.

Corrosion performance in short-term tests was verified over long exposure periods. During 25 d full immersion in 0.1 M NaCl, the OCP of $Al_{0.3}Cr_{0.5}Fe_2Mn_{0.25}Mo_{0.15}Ni_{1.5}Ti_{0.3}$ rose from -0.358 V_{SCE} to -0.283 V_{SCE} while the $Al_{0.3}Cr_{0.5}Fe_2Mn_0Mo_{0.15}Ni_{1.5}Ti_{0.3}$ OCP decreased from -0.022 V_{SCE} to -0.253 V_{SCE}. EIS measured at OCP for $Al_{0.3}Cr_{0.5}Fe_2Mn_0Mo_{0.15}Ni_{1.5}Ti_{0.3}$ (Figure 15[a]) shows impedance modulus (Z_{mod}) generally decreases after a 25 d immersion. A distinct change in the phase angle plot after immersion may suggest the loss of a CPE and a resultant change in oxide film composition or thickness. Contrastingly, $Al_{0.3}Cr_{0.5}Fe_2Mn_{0.25}Mo_{0.15}Ni_{1.5}Ti_{0.3}$ shows similar Z_{mod} and phase angle trends both before and after immersion (Figure 15[b]), which may suggest increasing stability of the passive film relative to $Al_{0.3}Cr_{0.5}Fe_2Mn_0Mo_{0.15}Ni_{1.5}Ti_{0.3}$. As the presence of Mn is the main compositional difference between the CCAs with other elemental concentrations remaining nearly constant, the increase in Z_{mod} in the low-frequency region of
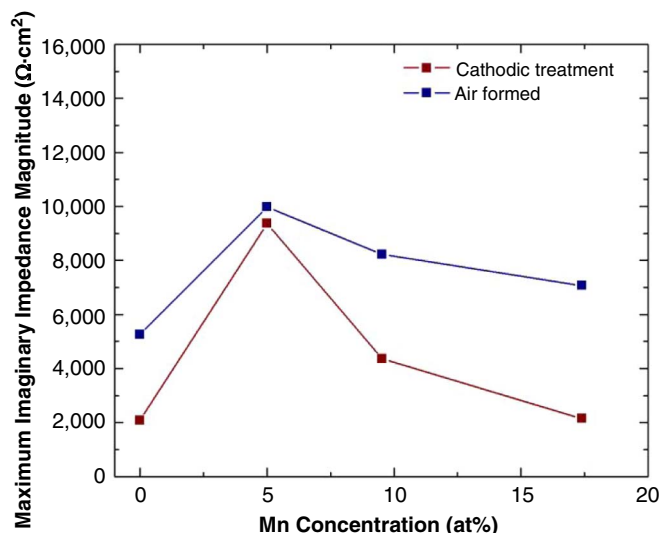
FIGURE 12. *Maximum imaginary components measured in situ at 1 Hz during polarization of post-cathodic treatment and air-formed oxides in 0.01 M NaCl.*

$Al_{0.3}Cr_{0.5}Fe_2Mn_{0.25}Mo_{0.15}Ni_{1.5}Ti_{0.3}$ between measurements before and after immersion that was not observed in $Al_{0.3}Cr_{0.5}Fe_2Mn_0Mo_{0.15}Ni_{1.5}Ti_{0.3}$ could be attributed to small additions of Mn. Table 6 shows the mass loss rates obtained during the immersion period. As the recorded mass loss rate for $Al_{0.3}Cr_{0.5}Fe_2Mn_{0.25}Mo_{0.15}Ni_{1.5}Ti_{0.3}$ approaches the precision of the scale, it was reported as trace; however, it may be safely considered lower than the rates of all other tested CCAs and comparable to 316L stainless steel. Beyond $Al_{0.3}Cr_{0.5}Fe_2Mn_{0.25}Mo_{0.15}Ni_{1.5}Ti_{0.3}$, the mass loss rate increases with higher Mn concentrations. The lower mass loss rate of $Al_{0.3}Cr_{0.5}Fe_2Mn_{0.25}Mo_{0.15}Ni_{1.5}Ti_{0.3}$ than $Al_{0.3}Cr_{0.5}Fe_2Mn_0Mo_{0.15}Ni_{1.5}Ti_{0.3}$ is consistent with the higher Z_{mod} values for $Al_{0.3}Cr_{0.5}Fe_2Mn_{0.25}Mo_{0.15}Ni_{1.5}Ti_{0.3}$ after 25 d of immersion. Limited pitting was visible on all alloys with some corrosion product present before rinsing. SEM images obtained after immersion (Figure 16) suggest that while pits are present in the

matrix, they are more prevalently found near the matrix-second phase interface. Pit growth across the interface into both phases roughly equally makes determination of an initiation site relative to the interface difficult, however, the symmetry of the pit across the interface suggests that initiation may occur at the interface rather than beside it.

3.3 | Elemental Dissolution Rates by Atomic Emission Spectroelectrochemistry

Figure 17 reports elemental dissolution currents (j_M) measured by AESEC during open-circuit exposure in 0.1 M NaCl pH 4. The breakdown morphologies and potential trends are consistent with those observed in Figure 9 despite changes in the zero current potential from the lack of $N_{2(g)}$ bubbling. Fe and Ni show the highest dissolution rates for all CCAs investigated. Cr initially shows a dissolution rate peak, then decays below the limit for reliable detection, suggesting passivation incorporating Cr^{3+}. Mo, Ti, and Al dissolution rates are below the detection limit. The sum of the elemental dissolution rates detected by AESEC ($\sum j_M$) for $Al_{0.3}Cr_{0.5}Fe_2Mn_{0.25}Mo_{0.15}Ni_{1.5}Ti_{0.3}$ at a near steady-state dissolution (1.8 ± 1.1 µA/cm^2) is lower than those of $Al_{0.3}Cr_{0.5}Fe_2Mn_0Mo_{0.15}Ni_{1.5}Ti_{0.3}$ (2.3 ± 0.9 µA/cm^2) and $Al_{0.3}Cr_{0.5}Fe_2Mn_1Mo_{0.15}Ni_{1.5}Ti_{0.3}$ (9.1 ± 2.9 µA/cm^2), which may indicate better corrosion resistance of $Al_{0.3}Cr_{0.5}Fe_2Mn_{0.25}Mo_{0.15}Ni_{1.5}Ti_{0.3}$ during open-circuit dissolution. For $Al_{0.3}Cr_{0.5}Fe_2Mn_1Mo_{0.15}Ni_{1.5}Ti_{0.3}$, j_{Mn} is 0.87 ± 0.04 µA/cm^2 at 600 s, close to j_{Fe} and j_{Ni} despite the lower concentration in the alloy. For the $Al_{0.3}Cr_{0.5}Fe_2Mn_{0.25}Mo_{0.15}Ni_{1.5}Ti_{0.3}$, the j_{Mn} at 600 s is only 0.04 ± 0.02 µA/cm^2, approximately 22 times lower than that of the $Al_{0.3}Cr_{0.5}Fe_2Mn_1Mo_{0.15}Ni_{1.5}Ti_{0.3}$.

The Mn dissolution rates measured in situ during upward polarization performed after a 600 s potential hold at -1.3 V$_{SCE}$ in $Al_{0.3}Cr_{0.5}Fe_2Mn_{0.25}Mo_{0.15}Ni_{1.5}Ti_{0.3}$ and $Al_{0.3}Cr_{0.5}Fe_2Mn_1Mo_{0.15}Ni_{1.5}Ti_{0.3}$ are compared alongside the electron current densities (j_e) in Figure 18. It should be noted that Mn dissolves below the breakdown potential, near 0.0 V$_{SCE}$, in $Al_{0.3}Cr_{0.5}Fe_2Mn_1Mo_{0.15}Ni_{1.5}Ti_{0.3}$, while Mn dissolution starts from the onset potential of transpassive dissolution for $Al_{0.3}Cr_{0.5}Fe_2Mn_{0.25}Mo_{0.15}Ni_{1.5}Ti_{0.3}$. j_{Mn} for $Al_{0.3}Cr_{0.5}Fe_2Mn_1Mo_{0.15}Ni_{1.5}Ti_{0.3}$ in both the passive and transpassive domain is

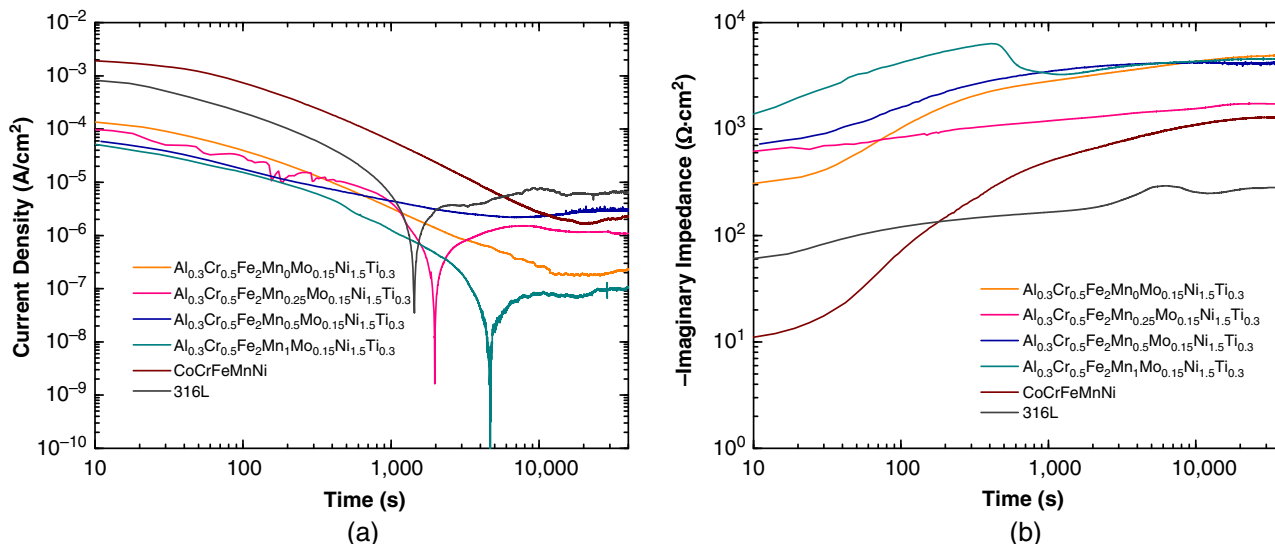**FIGURE 13.** *(a) Current density and (b) the imaginary impedance component measured in situ at 1 Hz during the application of a −0.25 V$_{SCE}$ potential for 40 ks in 0.01 M NaCl.*
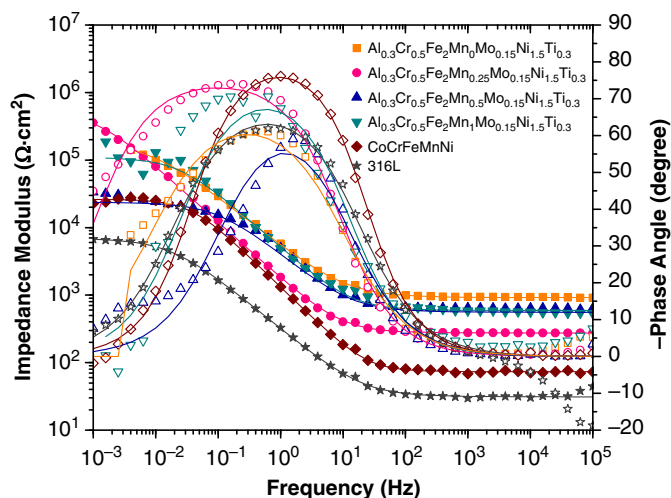
FIGURE 14. *Bode plot obtained in 0.01 M NaCl at −0.25 V_{SCE} for the oxide films grown during the preceding 40 ks potentiostatic hold fit with simplified Randles' circuits.*

Table 5. *Polarization Resistances and Phase Shifts (α) Determined by Circuit Model Fitting of EIS Obtained After a 40 ks Exposure to −0.25 V_{SCE} in 0.01 M NaCl*

Alloy	Polarization Resistance ($\Omega \cdot cm^2$)	α
$Al_{0.3}Cr_{0.5}Fe_2Mn_0Mo_{0.15}Ni_{1.5}Ti_{0.3}$	188,000	0.749
$Al_{0.3}Cr_{0.5}Fe_2Mn_{0.25}Mo_{0.15}Ni_{1.5}Ti_{0.3}$	533,000	0.838
$Al_{0.3}Cr_{0.5}Fe_2Mn_{0.5}Mo_{0.15}Ni_{1.5}Ti_{0.3}$	23,300	0.787
$Al_{0.3}Cr_{0.5}Fe_2Mn_1Mo_{0.15}Ni_{1.5}Ti_{0.3}$	109,000	0.834
CoCrFeMnNi	26,200	0.908
316L	116,000	0.779

approximately two orders of magnitude higher than for $Al_{0.3}Cr_{0.5}Fe_2Mn_{0.25}Mo_{0.15}Ni_{1.5}Ti_{0.3}$.

Dissolution currents of $Al_{0.3}Cr_{0.5}Fe_2Mn_{0.25}Mo_{0.15}Ni_{1.5}Ti_{0.3}$ constituent elements monitored at an applied potential of −0.2 V_{SCE} in 0.1 M NaCl pH 4 (Figure 19) are highest for Fe and Ni, where dissolution peaks are visible in the initial several hundreds of seconds. Traditional passivators such as Ti, Cr, Al, and Mo are below the detection limit. Notably, the Mn dissolution rate is significantly below Fe and Ni and is comparable to the passivating elements. The elemental dissolution is reasonably consistent with the thermodynamic prediction at pH 4, −0.2 V_{SCE} shown in Table 7.

3.4 | Analysis of Passive Film Compositions by X-Ray Photoelectron Spectroscopy

High-resolution XPS spectra obtained after the 40 ks potentiostatic hold experiments (Figure 13) suggest formation of a passive film consisting of both oxides and hydroxides. The XPS spot size encompasses both the matrix and second phase. Selected fits for Ti, Cr, and Al, three important passivating elements, along with crude Mn fits, are shown in Figure 20. Chemically shifted (oxidized atoms) peaks are utilized in the

calculation of passive film cation fractions and signal attributable to bulk metal peaks were neglected. In the case of Mo, Al, and Mn, it is possible to see a chemical shift and thus ascertain cation fractions, but it is not feasible to further deconvolute the oxidized or metal peaks where necessary due to low signal and high levels of noise. A crude fit of the Mn $2p_{1/2}$ spectrum at the maximum possible concentration not exceeding XPS signal noise was applied as previously utilized for other CCAs.[14] Any analysis of Mn cation fractions or surface enhancement is intended as an upper bound to a range of possible Mn concentrations.

Cation fractions from the high-resolution spectra are shown in Figure 21 and Table 8. The passive film of $Al_{0.3}Cr_{0.5}Fe_2Mn_{0.25}Mo_{0.15}Ni_{1.5}Ti_{0.3}$, which exhibits the best corrosion resistance for the alloy system explored herein, is enriched in Ti, Al, and Cr relative to the alloy composition. Ti constitutes the majority of the passive film and may be presumed to be enriched in the passive film formed over the second phase given preferential segregation into the second phase of the microstructure. Although all elements are present in both phases, Al, Ni, and Ti are enriched in the second phase while Co, Fe, Mn, and Mo are predominant found in the matrix (Figure 4, Table 3).

In the case of Fe and Cr, a proportion of the spectra is indexed to $FeCr_2O_4$, manually preserving the stoichiometric ratio between normalized intensities. The oxidized species of both Ni and Al are accompanied by significant intensities at binding energies corresponding to elemental zero valence state metal peaks. The high dissolution rates of Fe and Ni observed with AESEC during a potentiostatic hold under similar conditions (Figure 19) may be correlated to the depletion of those elements measured by XPS. Cr and Ti dissolution rates were under the detection limit which supports the notion of the enrichment of Cr and Ti indicated by XPS (Figure 21, Table 8).

The passive film of $Al_{0.3}Cr_{0.5}Fe_2Mn_1Mo_{0.15}Ni_{1.5}Ti_{0.3}$ is enriched in Ti, Cr, and, at a small ratio, Mo. Unlike in the case of $Al_{0.3}Cr_{0.5}Fe_2Mn_{0.25}Mo_{0.15}Ni_{1.5}Ti_{0.3}$, Al is depleted in the passive film. It should be noted that Mn is suggested to be depleted based on the low XPS signal in both CCAs despite the high bulk content in $Al_{0.3}Cr_{0.5}Fe_2Mn_1Mo_{0.15}Ni_{1.5}Ti_{0.3}$. Elemental fractions for Mn in each CCA's passive film are no greater than 0.18 at% and 0.64 at% for $Al_{0.3}Cr_{0.5}Fe_2Mn_{0.25}Mo_{0.15}Ni_{1.5}Ti_{0.3}$ and $Al_{0.3}Cr_{0.5}Fe_2Mn_1Mo_{0.15}Ni_{1.5}Ti_{0.3}$, respectively, suggesting roughly similar depletion factors. Fe is suggested to be present in lower proportions in the passive film of $Al_{0.3}Cr_{0.5}Fe_2Mn_1Mo_{0.15}Ni_{1.5}Ti_{0.3}$ than in the film of $Al_{0.3}Cr_{0.5}Fe_2Mn_{0.25}Mo_{0.15}Ni_{1.5}Ti_{0.3}$. Al and Ti are observed at lower proportions with increased Mn content in the alloy. Contrastingly, the proportions of Cr and Mo cations increase in the $Al_{0.3}Cr_{0.5}Fe_2Mn_1Mo_{0.15}Ni_{1.5}Ti_{0.3}$ spectra. These hint at the importance of Ti, Al, Cr, and Mo and show the elusiveness of Mn. Nevertheless, evidence is strong for the optimization of Mn over several environments and evaluated by five different methods.

DISCUSSION

4.1 | Microstructural Aspects Related to Mn

Small additions of Mn are suggested to increase the homogeneity of the microstructure. Although none of the microstructures explored herein is suggested to be single-phase, the increased likelihood of single-phase stability may be quantified with increases in configurational entropy and decreases in the average radius mismatch. Both the Ω indicator proposed by Yang and Zhang[6] and the Φ indicator proposed
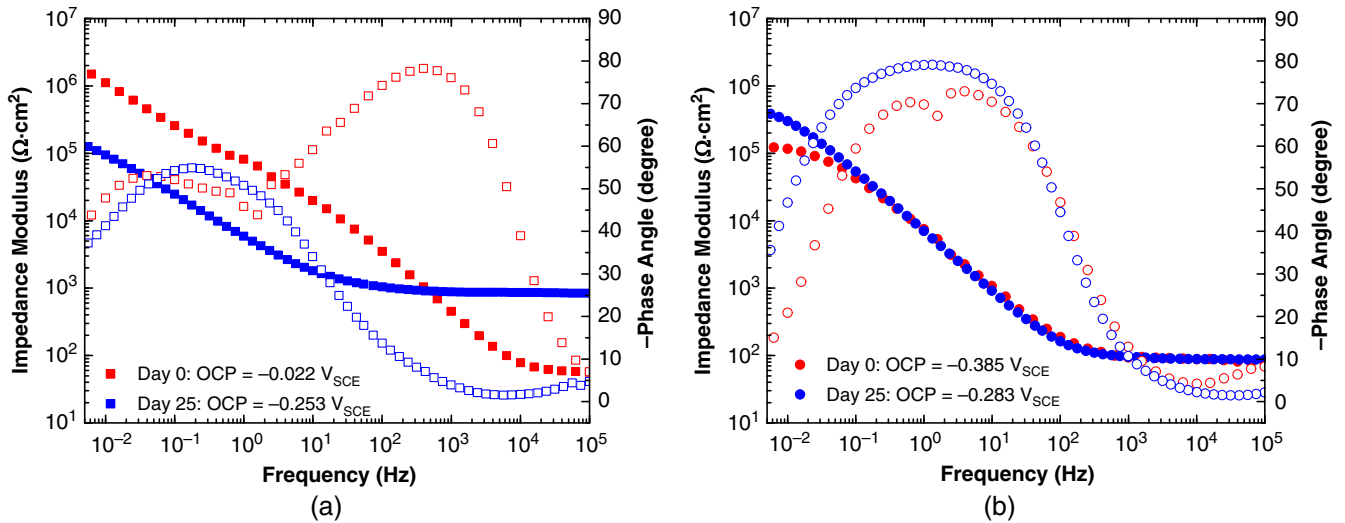
FIGURE 15. *Bode plot of (a) $Al_{0.3}Cr_{0.5}Fe_2Mn_0Mo_{0.15}Ni_{1.5}Ti_{0.3}$ and (b) $Al_{0.3}Cr_{0.5}Fe_2Mn_{0.25}Mo_{0.15}Ni_{1.5}Ti_{0.3}$ obtained prior to and directly following 25 d immersion in 0.1 M NaCl. Spectra were measured at the OCPs indicated in the figure legends.*

Table 6. *Mass Loss Rates Obtained During Immersion in 0.1 M NaCl*

Alloy	Mass Loss Rate (mg/cm²/y)	Penetration Rate (µm/y)
$Al_{0.3}Cr_{0.5}Fe_2Mn_0Mo_{0.15}Ni_{1.5}Ti_{0.3}$	10.1	13.0
$Al_{0.3}Cr_{0.5}Fe_2Mn_{0.25}Mo_{0.15}Ni_{1.5}Ti_{0.3}$	Trace	Trace
$Al_{0.3}Cr_{0.5}Fe_2Mn_{0.5}Mo_{0.15}Ni_{1.5}Ti_{0.3}$	2.2	2.9
$Al_{0.3}Cr_{0.5}Fe_2Mn_1Mo_{0.15}Ni_{1.5}Ti_{0.3}$	7.8	10.0
CoCrFeMnNi	9.5	11.9
316L	Trace	Trace

(A) Mass changes in $Al_{0.3}Cr_{0.5}Fe_2Mn_{0.25}Mo_{0.15}Ni_{1.5}Ti_{0.3}$ and 316L approached the tolerance of the scale and were reported as trace.

by King, et al.,[4] increase with Mn content (Table 2). Single-phase stability is predicted for all CCAs by Ω and ΔS_{mix} terms but the high enthalpy of mixing between Ti and Ni keeps the Φ term below King's proposed threshold.[4] A high lattice mismatch term likely prevents complete solubility, as δ is still above the 4.7% threshold proposed by Feng, et al.,[1] for all CCAs, which likely causes phase segregation as single-phase CCAs typically satisfy both thermodynamic indicator and δ thresholds.[1] Phase contrast was observed with Mn concentrations approaching 20 at%, validating calculations suggesting a Mn concentration of over 75 at%, well outside the feasible range for corrosion resistant design, would be necessary to obtain a δ value below 4.7%. Although the single-phase stability predicted by CALPHAD modeling in Figure 2 was not observed experimentally, the widening temperature range of the single-phase fcc
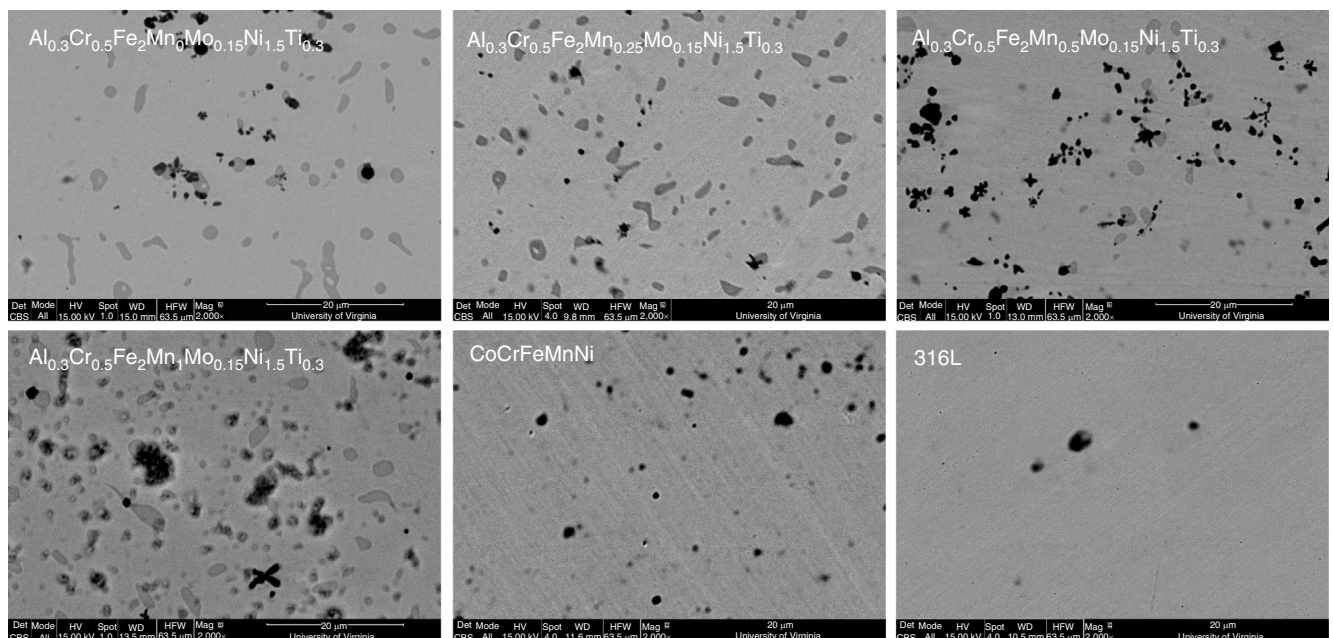

FIGURE 16. *BSE images of CCA pit morphology after immersion in 0.1 M NaCl.*
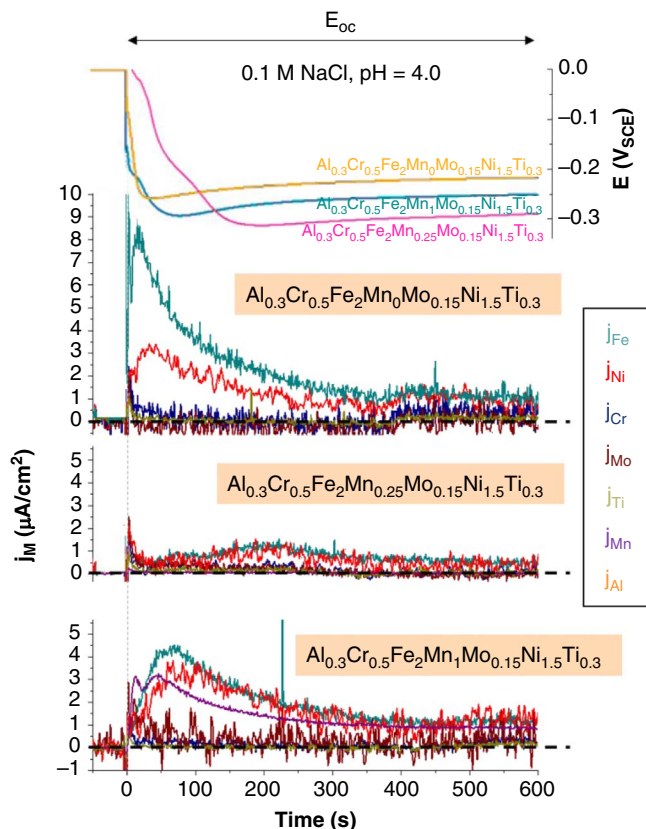
FIGURE 17. *Elemental dissolution rates monitored by AESEC during exposure to OCP of $Al_{0.3}Cr_{0.5}Fe_2Mn_0Mo_{0.15}Ni_{1.5}Ti_{0.3}$, $Al_{0.3}Cr_{0.5}Fe_2Mn_{0.25}Mo_{0.15}Ni_{1.5}Ti_{0.3}$, and $Al_{0.3}Cr_{0.5}Fe_2Mn_{0.25}Mo_{0.15}Ni_{1.5}Ti_{0.3}$ in 0.1 M NaCl pH 4.*
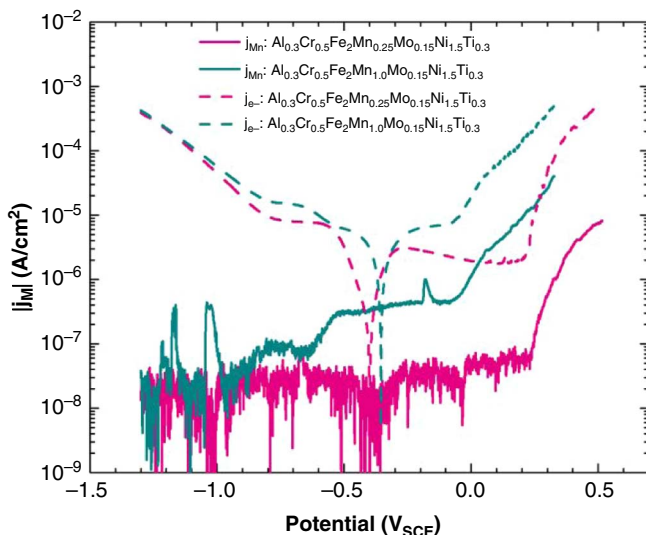

FIGURE 18. *Mn (j_{Mn}) and electron current density (j_e) of $Al_{0.3}Cr_{0.5}Fe_2Mn_{0.25}Mo_{0.15}Ni_{1.5}Ti_{0.3}$ and $Al_{0.3}Cr_{0.5}Fe_2Mn_{1.0}Mo_{0.15}Ni_{1.5}Ti_{0.3}$ alloys monitored by AESEC during potentiodynamic polarization following a 600 s applied potential at −1.3 V_{SCE} in 0.1 M NaCl pH 4.*

region may suggest increased stability of the fcc phase with increasing Mn concentration below 20 at%.

Although multiple phases are present, EDS suggests the CCAs with higher Mn concentration have improved compositional homogeneity (Figure 4, Table 3). Most noticeably, the ratio of Ti
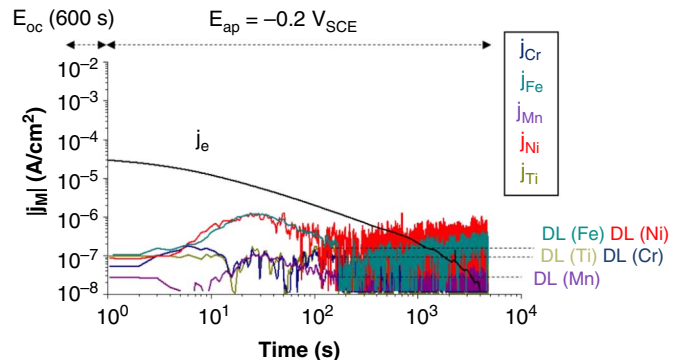

FIGURE 19. *Elemental dissolution rates of $Al_{0.3}Cr_{0.5}Fe_2Mn_{0.25}Mo_{0.15}Ni_{1.5}Ti_{0.3}$ during a 4 ks potentiostatic hold at −0.2 V_{SCE} following a 600 s exposure to OCP in 0.1 M NaCl pH 4. j_e indicates the electron current density. Horizontal dashed lines indicate the detection limit (DL) for each element. j_{Al} and j_{Mo} were below the detection limits and are not plotted.*

Table 7. *Elemental Summary of Open-Circuit Dissolution in 0.1 M NaCl at pH 4 Monitored by AESEC*[(A)]

Alloy		OCP (−0.3 V_{SCE} to −0.2 V_{SCE})
$Al_{0.3}Cr_{0.5}Fe_2Mn_0Mo_{0.15}Ni_{1.5}Ti_{0.3}$		Initial Fe, Ni dissolution
$Al_{0.3}Cr_{0.5}Fe_2Mn_{0.25}Mo_{0.15}Ni_{1.5}Ti_{0.3}$		Initial Fe, Ni dissolution
$Al_{0.3}Cr_{0.5}Fe_2Mn_1Mo_{0.15}Ni_{1.5}Ti_{0.3}$		Initial Fe, Ni, Mn dissolution
Thermodynamics (Hydra Medusa)	Soluble	$Cr(OH)^{2+}$, Mn^{2+}, Ni^{2+}, Fe^{2+}, Al^{3+}
	Nonsoluble	$MoO_2(cr)$, $TiO_2(cr)$

[(A)] Thermodynamically stable species in 0.1 M NaCl pH 4 at 25°C predicted by Hydra Medusa[†] software using its default database are provided for comparative purposes.

concentration in the second phase relative to the matrix is generally lower in alloys containing Mn. A decreased concentration gradient between the matrix and the second phase may minimize local chemical heterogeneity, particularly near the interface where pits often form (Figure 15). Given that Ti is suggested by XPS to play a key role in passivation, the effect may contribute to vulnerability to localized corrosion with the chemical heterogeneity and structural disorder contributing to a susceptible site.

Even though Mn promotes homogeneous distribution of passivating elements, it has its own detrimental effects as an oxide film former. Mn_2O_3 in Fe-Mn alloys and elsewhere forms an unprotective oxide marked by fast ionic transport rates and internal voiding during oxidation. Poor corrosion resistance is seen in many binary alloys.[73] Instability of Mn in the passive films may be driven in part by the low solubility of Mn oxides with other oxides including Al_2O_3 and Cr_2O_3.[15] This accounts for the poor polarization resistance in high Mn alloys assuming Mn oxides form, which is addressed below.

4.2 | Thermodynamic Aspects of Oxides Formed on Al-Cr-Fe-Mn-Mo-Ni-Ti Alloys

The high number of constituent elements greatly increases the range of oxide species that may be thermodynamically stable.
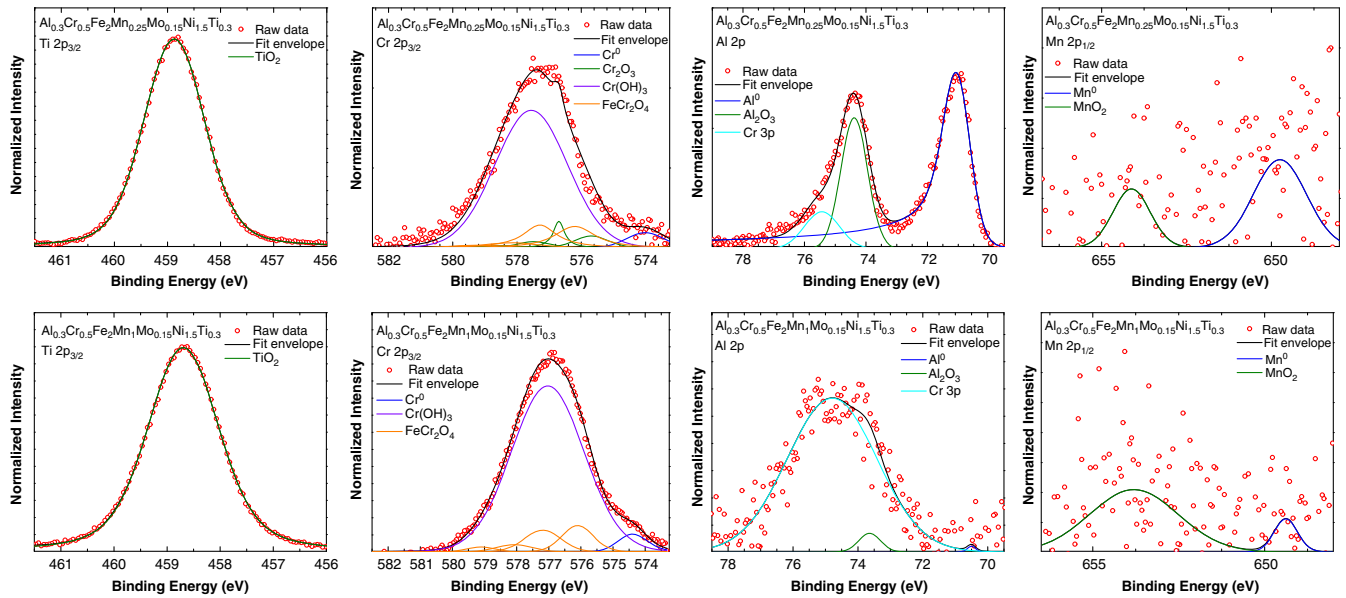
FIGURE 20. *Deconvoluted XPS spectra and fits for key passivating elements and Mn.*
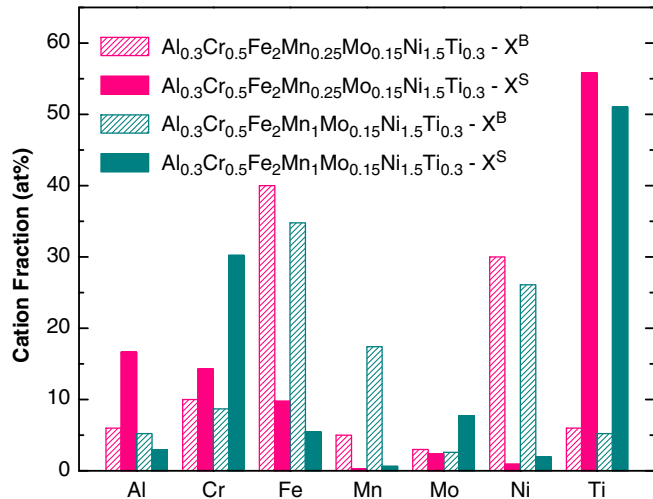

FIGURE 21. *Passivated cation fractions calculated from deconvolution of XPS data. Passivated cation fractions obtained via XPS (X^S) for $Al_{0.3}Cr_{0.5}Fe_2Mn_{0.25}Mo_{0.15}Ni_{1.5}Ti_{0.3}$ and $Al_{0.3}Cr_{0.5}Fe_2Mn_{0.25}Mo_{0.15}Ni_{1.5}Ti_{0.3}$ are compared to their alloy compositions (X^B) to highlight elemental enrichment or depletion in the passive films.*

Three types of oxides are possible: kinetically limited solute captured, thermodynamically stable solid solutions and specific stoichiometric oxides such as spinels. Ni, Mo, and Mn were not found in oxides in high enough cation fraction to accommodate spinels given to preserve stoichiometric ratios. Other specific oxides that cannot be ruled out based on thermodynamic stability include but are not limited to $FeCr_2O_4$, $Cr_2Ti_2O_7$, $TiAl_2O_5$, and $TiFeO_3$.[74] Each metal may passivate in multiple potential valence states, leading to a wide range in potential species. Furthermore, interaction with water also introduces the possibility of forming hydroxide or oxyhydroxide species. In addition to differences in free energy of formation, the stable oxide for a given metal may be altered by the local activity of oxygen.

The predicted oxide stoichiometry, as suggested by the lowest free energy of formation for each metal in the system is Al_2O_3, Cr_2O_3, Fe_2O_3, Mn_3O_4, MoO_2, NiO, and TiO_2.[75] Such insoluble oxide species are present in the potential-pH diagrams for all pure elements found in the tested alloys, though applied potential and solution environment may alter the most thermodynamically stable species and often are not proposed to be the stable species under the tested conditions.[76]

Although the formation energy of Mn_3O_4 (−197.7 kJ/mol) is more negative than that of Mn_2O_3 (−194.2 kJ/mol), MnO_2

Table 8. *Cation Fractions Determined by XPS and Surface Enrichment Calculations for Each Element*

Alloy	$Al_{0.3}Cr_{0.5}Fe_2Mn_{0.25}Mo_{0.15}Ni_{1.5}Ti_{0.3}$		$Al_{0.3}Cr_{0.5}Fe_2Mn_1Mo_{0.15}Ni_{1.5}Ti_{0.3}$	
Metal	X^S (at%)	f	X^S (at%)	f
Al	16.6	2.77	3.0	0.58
Cr	14.3	1.43	30.2	3.47
Fe	9.7	0.24	5.5	0.16
Mn	0.3	0.06	0.6	0.04
Mo	2.3	0.77	7.7	2.95
Ni	0.9	0.03	2.0	0.08
Ti	55.8	9.30	51.0	9.78

(−174.2 kJ/mol), and MnO (−190.4 kJ/mol), the similar magnitudes suggest the in prevailing oxide species may vary by environment.[75] The potential-pH diagram suggests applied potential ranges for the stability of Mn_3O_4, Mn_2O_3, and MnO_2 depend on the potential along with $Mn(OH)_2$.[77] Mn may also be a constituent in multi-element oxides. Although there are multiple possible ordered tertiary oxides that could be thermodynamically stable, the low concentrations of Mn in both the bulk alloy and in the passive film make the formation of such compounds unlikely. Therefore, limited Mn solubility in other oxide structures or trapping near the interface may be more likely than a defined Mn oxide or possibly beneficial Mn-containing tertiary oxide such as Mn_3O_4, $MnFe_2O_4$, or $MnAl_2O_4$.

4.3 | Experimental Validation and Kinetic Limitations

While thermodynamic predictions may determine the most energetically favorable oxide structure, such predictions are often not reliable in experimental settings, particularly given the complications of a seven-element alloy space. Through combinations of XPS characterization of the passive film and AESEC characterization of the dissolution rates, the fate of individual elements during the passivation process may be determined. Each alloy and phase subcomponent may contain similar concentrations of passivating elements Cr, Ti, and Al (Tables 1 and 3) yet corrosion performance is distinctly dependent on Mn. Changes in the enrichment of individual element between the CCAs help elucidate the effect of Mn concentration on the elements and their role in corrosion resistance. A complexity here is the accounting for the oxide formed over two phases, where Mn concentration affects the degree of partitioning between an Al, Ti, Ni phase and the matrix enriched in Cr, Mo, and Fe. The Ti enrichment factor in the $Al_{0.3}Cr_{0.5}Fe_2Mn_1Mo_{0.15}Ni_{1.5}Ti_{0.3}$ passive film is slightly lower than in $Al_{0.3}Cr_{0.5}Fe_2Mn_{0.25}Mo_{0.15}Ni_{1.5}Ti_{0.3}$ and is compensated by increasing Cr passivation (Figure 21, Table 8). Corrosion resistance may be enhanced by having a key passivating element, either Cr or Ti, enriched in both the matrix and second phase regions of the microstructure.

Within the $Al_{0.3}Cr_{0.5}Fe_2Mn_xMo_{0.15}Ni_{1.5}Ti_{0.3}$ system, the optimal Mn concentration for corrosion resistance is suggested to be near 5 at%. Compositions above 5 at% Mn may decrease corrosion resistance, but do not leave the alloys as vulnerable to corrosion as compositions near 20 at%. Therefore, the Mn concentrations can be slightly increased to further decrease alloy cost and density or to target mechanical ductility, however, the composition ranges near 25 at% that have been suggested to be necessary to demonstrate significant twinning-induced plasticity in Fe-Mn-Al steels[78] would significantly harm the corrosion resistance of the alloy. Utilizing Mn as a partial replacement for Ni would reduce the alloy density and cost while preserving some of the austenitic stability. However, Mn may not be as effective of an austenitic stabilizer as Ni under many conditions[37] and the corrosion resistance of a CCA series with increasing Mn content and decreasing Ni content remains unexplored.

CONCLUSIONS

➢ Four Al- and Ti-containing CCAs with varying Mn contents were synthesized and evaluated for corrosion resistance. All CCAs possessed a two-phase microstructure with Al, Ni, and Ti enriched in the second phase. Mn had similar concentrations across both phases and was the only element not significantly enriched or depleted in the second phase. Furthermore, the

CCAs with Mn tended to have lower magnitudes of compositional difference between phases than the CCA without, potentially affecting the formation of pitting sites.

➢ In dilute chloride solutions, adding 5 at% Mn increased pitting and repassivation potentials and improved overall corrosion resistance of the oxide films formed on reduced metal surfaces, challenging traditional intuition that suggests completely avoiding Mn. Similar trends were verified with increased chloride concentrations and by evaluating the air-formed passive layer. In a CCA with a high Mn concentration, the dissolution rates of both Mn and other constituent elements increased, and overall corrosion resistance decreased.

➢ Both Ti and Cr appear to play key roles in passivation based upon their surface enrichment, although the structure of the complex oxide remains undetermined. Mn was significantly depleted from the passive films.

➢ Similar intuition may be utilized for the optimization of Mn in other CCA systems containing Al and Ti as the alloy space grows in prominence with the increasing demand for low cost, lightweight CCAs.

References

1. R. Feng, C. Lee, M. Mathes, T.T. Zuo, S. Chen, J. Hawk, Y. Zhang, P. Liaw, *Entropy* 18 (2016): p. 333.
2. J. Qi, A.M. Cheung, S.J. Poon, *Sci. Rep.* 9, 1 (2019): p. 15501.
3. D.B. Miracle, O.N. Senkov, *Acta Mater.* 122 (2017): p. 448-511.
4. D.J.M. King, S.C. Middleburgh, A.G. McGregor, M.B. Cortie, *Acta Mater.* 104 (2016): p. 172-179.
5. A. Miedema, *Philips Tech. Rev.* 33, 6 (1973): p. 149-160.
6. X. Yang, Y. Zhang, *Mater. Chem. Phys.* 132, 2 (2012): p. 233-238.
7. J. Qi, A.M. Cheung, S.J. Poon, "Navigating the Complex Compositional Landscape of High-Entropy Alloys" (2021): arXiv:2011.14403v2.
8. E. Menou, F. Tancret, I. Toda-Caraballo, G. Ramstein, P. Castany, E. Bertrand, N. Gautier, P.E.J. Rivera Díaz-Del-Castillo, *Scr. Mater.* 156 (2018): p. 120-123.
9. C. Varvenne, A. Luque, W.A. Curtin, *Acta Mater.* 118 (2016): p. 164-176.
10. P. Lu, J.E. Saal, G.B. Olson, T. Li, O.J. Swanson, G.S. Frankel, A.Y. Gerard, K.F. Quiambao, J.R. Scully, *Scr. Mater.* 153 (2018): p. 19-22.
11. Y. Qiu, M.A. Gibson, H.L. Fraser, N. Birbilis, *Mater. Sci. Technol.* 31, 10 (2015): p. 1235-1243.
12. Y. Qiu, S. Thomas, M.A. Gibson, H.L. Fraser, N. Birbilis, *npj Mater. Degrad.* 1, 1 (2017): article 15.
13. K.F. Quiambao, S.J. McDonnell, D.K. Schreiber, A.Y. Gerard, K.M. Freedy, P. Lu, J.E. Saal, G.S. Frankel, J.R. Scully, *Acta Mater.* 164 (2019): p. 362-376.
14. A.Y. Gerard, J. Han, S.J. McDonnell, K. Ogle, E.J. Kautz, D.K. Schreiber, P. Lu, J.E. Saal, G.S. Frankel, J.R. Scully, *Acta Mater.* 198 (2020): p. 121-133.
15. K. Wang, J. Han, A.Y. Gerard, J.R. Scully, B.-C. Zhou, *npj Mater. Degrad.* 4, 1 (2020): article 35.
16. Z. Tang, L. Huang, W. He, P.K. Liaw, *Entropy* 16, 2 (2014): p. 895-911.
17. J.R. Scully, S.B. Inman, A.Y. Gerard, C.D. Taylor, W. Windl, D.K. Schreiber, P. Lu, J.E. Saal, G.S. Frankel, *Scr. Mater.* 188 (2020): p. 96-101.

18. D. Yang, Y. Liu, H. Jiang, M. Liao, N. Qu, T. Han, Z. Lai, J. Zhu, *J. Alloys Compd.* 823 (2020): p. 153729.

19. D.H. Xiao, P.F. Zhou, W.Q. Wu, H.Y. Diao, M.C. Gao, M. Song, P.K. Liaw, *Mater. Des.* 116 (2017): p. 438-447.

20. E. Osei-Agyemang, G. Balasubramanian, *npj Mater. Degrad.* 3, 1 (2019): article 20.

21. C.P. Lee, C.C. Chang, Y.Y. Chen, J.W. Yeh, H.C. Shih, *Corros. Sci.* 50, 7 (2008): p. 2053-2060.

22. B.-y. Li, K. Peng, A.-p. Hu, L.-p. Zhou, J.-j. Zhu, D.-y. Li, *Trans. Nonferrous Met. Soc. China* 23, 3 (2013): p. 735-741.

23. Y. Qiu, S. Thomas, D. Fabijanic, A.J. Barlow, H.L. Fraser, N. Birbilis, *Mater. Des.* 170 (2019): p. 107698.

24. Y. Shi, L. Collins, R. Feng, C. Zhang, N. Balke, P. Liaw, B. Yang, *Corros. Sci.* 133 (2018): p. 121-130.

25. K. Ishikawa, I. Ohnuma, R. Kainuma, K. Aoki, K. Ishida, *J. Alloys Compd.* 367, 1 (2004): p. 2-9.

26. D. Choudhuri, T. Alam, T. Borkar, B. Gwalani, A.S. Mantri, S.G. Srinivasan, M.A. Gibson, R. Banerjee, *Scr. Mater.* 100 (2015): p. 36-39.

27. Z.-S. Nong, Y.-N. Lei, J.-C. Zhu, *Intermetallics* 101 (2018): p. 144-151.

28. Y. Shi, L. Collins, N. Balke, P.K. Liaw, B. Yang, *Appl. Surf. Sci.* 439 (2018): p. 533-544.

29. Y. Shi, L. Collins, R. Feng, C. Zhang, N. Balke, P.K. Liaw, B. Yang, *Corros. Sci.* 133 (2018): p. 120-131.

30. B. Cantor, I.T.H. Chang, P. Knight, A.J.B. Vincent, *Mater. Sci. Eng. A* 375-377 (2004): p. 213-218.

31. J.A. Ober, "Mineral Commodity Summaries," U.S. Geological Survey, 2018, p. 204.

32. S. Singerling, C. Tuck, *Minerals Yearbook: Metals and Minerals*, vol. 1 (Reston, VA: USGS, 2018), p. 25.21-25.14.

33. Y.L. Zhao, T. Yang, J.H. Zhu, D. Chen, Y. Yang, A. Hu, C.T. Liu, J.J. Kai, *Scr. Mater.* 148 (2018): p. 51-55.

34. R.K. Mishra, R.R. Shahi, *J. Magn. Magn. Mater.* 442 (2017): p. 218-223.

35. Y. Deng, C.C. Tasan, K.G. Pradeep, H. Springer, A. Kostka, D. Raabe, *Acta Mater.* 94 (2015): p. 124-133.

36. D. Raabe, D. Ponge, O. Dmitrieva, B. Sander, *Adv. Eng. Mater.* 11, 7 (2009): p. 547-555.

37. R.L. Klueh, P.J. Maziasz, E.H. Lee, *Mater. Sci. Eng. A* 102, 1 (1988): p. 115-124.

38. M.H. Brown, W.B. Delong, *Ind. Eng. Chem.* 39, 10 (1947): p. 1248-1254.

39. M.A. Baker, J.E. Castle, *Corros. Sci.* 34, 4 (1993): p. 667-682.

40. Y.S. Zhang, X.M. Zhu, *Corros. Sci.* 41, 9 (1999): p. 1817-1833.

41. S. Fajardo, I. Llorente, J.A. Jiménez, J.M. Bastidas, D.M. Bastidas, *Corros. Sci.* 154 (2019): p. 246-253.

42. X.M. Zhu, Y.S. Zhang, *Corrosion* 54, 01 (1998): p. 98010003.

43. J. Bosch, U. Martin, W. Aperador, J.M. Bastidas, J. Ress, D.M. Bastidas, *Materials* 14, 2 (2021): p. 425.

44. K. Park, H. Kwon, *Electrochim. Acta* 55, 9 (2010): p. 3421-3427.

45. J. Yang, J. Wu, C.Y. Zhang, S.D. Zhang, B.J. Yang, W. Emori, J.Q. Wang, *J. Alloys Compd.* 819 (2020): p. 152943.

46. H. Torbati-Sarraf, M. Shabani, P.D. Jablonski, G.J. Pataky, A. Poursaee, *Mater. Des.* 184 (2019): p. 108170.

47. K.Y. Tsai, M.H. Tsai, J.W. Yeh, *Acta Mater.* 61, 13 (2013): p. 4887-4897.

48. V. Kukshal, A. Patnaik, I.K. Bhat, *IOP Conf. Ser. Mater. Sci. Eng.* 377 (2018): p. 012023.

49. S.-K. Wong, T.-T. Shun, C.-H. Chang, C.-F. Lee, *Mater. Chem. Phys.* 210 (2018): p. 146-151.

50. M.J. Kim, J. Kim, *Int. J. Electrochem. Sci.* 10 (2015): p. 6872-6885.

51. A. Rodriguez, J.H. Tylczak, M. Ziomek-Moroz, *ECS Trans.* 77, 11 (2017): p. 741-752.

52. Y. Qiu, R. Liu, T. Gengenbach, O. Gharbi, S. Choudhary, S. Thomas, H.L. Fraser, N. Birbilis, *npj Mater. Degrad.* 4, 1 (2020): article 7.

53. J. Han, X. Li, A.Y. Gerard, P. Lu, J.E. Saal, G.S. Frankel, K. Ogle, J.R. Scully, *J. Electrochem. Soc.* 168, 5 (2021): p. 051508.

54. L. Kjellqvist, M. Selleby, *J. Phase Equilib. Diffus.* 31, 2 (2010): p. 113-134.

55. L. Kjellqvist, M. Selleby, *J. Alloys Compd.* 507, 1 (2010): p. 84-92.

56. L. Kjellqvist, M. Selleby, *Int. J. Mater. Res.* 101, 10 (2010): p. 1222-1231.

57. H. Luo, Z. Li, A.M. Mingers, D. Raabe, *Corros. Sci.* 134 (2018): p. 131-139.

58. H. Xiao, Y. Liu, K. Wang, Z. Wang, T. Hu, T. Fan, L. Ma, P. Tang, *Acta Metall. Sin. (English Lett.)* 34 (2020): p. 455-464.

59. Thermocalc Software Version 2019b, TCHEA High-Entropy Alloys v9.1.

60. E. Clementi, D.L. Raimondi, W.P. Reinhardt, *J. Chem. Phys.* 47, 4 (1967): p. 1300-1307.

61. A. Takeuchi, A. Inoue, *Mater. Trans.* 46, 12 (2005): p. 2817-2829.

62. K. Lutton, K. Gusieva, N. Ott, N. Birbilis, J.R. Scully, *Electrochem. Commun.* 80 (2017): p. 44-47.

63. B. Hirschorn, M.E. Orazem, B. Tribollet, V. Vivier, I. Frateur, M. Musiani, *J. Electrochem. Soc.* 157, 12 (2010): p. C452.

64. B. Hirschorn, M.E. Orazem, B. Tribollet, V. Vivier, I. Frateur, M. Musiani, *J. Electrochem. Soc.* 157, 12 (2010): p. C458.

65. ASTM G1-03(2017)e1, "Standard Practice for Preparing, Cleaning, and Evaluating Corrosion Test Specimens" (West Conshohocken, PA: ASTM International, 2017).

66. K. Ogle, *Corrosion* 75, 12 (2019): p. 1398-1419.

67. U.-E. Charles-Granville, C. Liu, J.R. Scully, R.G. Kelly, *J. Electrochem. Soc.* 167, 11 (2020): p. 111507.

68. M.C. Biesinger, L.W.M. Lau, A.R. Gerson, R.S.C. Smart, *Appl. Surf. Sci.* 257, 3 (2010): p. 887-898.

69. J. Baltrusaitis, B. Mendoza-Sanchez, V. Fernandez, R. Veenstra, N. Dukstiene, A. Roberts, N. Fairley, *Appl. Surf. Sci.* 326 (2015): p. 151-161.

70. M.C. Biesinger, B.P. Payne, A.P. Grosvenor, L.W.M. Lau, A.R. Gerson, R.S.C. Smart, *Appl. Surf. Sci.* 257, 7 (2011): p. 2717-2730.

71. L. Wang, D. Mercier, S. Zanna, A. Seyeux, M. Laurent-Brocq, L. Perrière, I. Guillot, P. Marcus, *Corros. Sci.* 167 (2020): p. 108507.

72. J.E. Castle, K. Asami, *Surf. Interface Anal.* 36, 3 (2004): p. 220-224.

73. S. Sahu, O. Swanson, T. Li, A. Gerard, J. Scully, G. Frankel, *Electrochim. Acta* 354 (2020): p. 136749.

74. Thermocalc Software Version 2019b, TCFE Steels/Fe-Alloys v9.1.

75. A. Jain, S.P. Ong, G. Hautier, W. Chen, W.D. Richards, S. Dacek, S. Cholia, D. Gunter, D. Skinner, G. Ceder, K.A. Persson, *APL Mater.* 1, 1 (2013): p. 011002.

76. T.C. Kaspar, D.K. Schreiber, S.R. Spurgeon, M.E. McBriarty, G.M. Carroll, D.R. Gamelin, S.A. Chambers, *Adv. Mater.* 28, 8 (2016): p. 1616-1622.

77. M. Pourbaix, *Atlas of Electrochemical Equilibria in Aqueous Solutions* (Houston, TX: NACE International, 1974).

78. O. Grässel, L. Krüger, G. Frommeyer, L.W. Meyer, *Int. J. Plasticity* 16, 10 (2000): p. 1391-1409.